

Second-order accurate derivatives and integration schemes for meshfree methods

Qinglin Duan^{1,*}, Xikui Li^{1,2}, Hongwu Zhang^{1,2} and Ted Belytschko³

¹*Department of Engineering Mechanics, Dalian University of Technology, Dalian, Liaoning 116024, China*

²*The State Key Laboratory of Structural Analysis for Industrial Equipment, Dalian University of Technology, Dalian, Liaoning 116024, China*

³*Department of Mechanical Engineering, Northwestern University, Evanston, IL 60208-3111, USA*

SUMMARY

The consistency condition for the nodal derivatives in traditional meshfree Galerkin methods is only the differentiation of the approximation consistency (DAC). One missing part is the consistency between a nodal shape function and its derivatives in terms of the divergence theorem in numerical forms. In this paper, a consistency framework for the meshfree nodal derivatives including the DAC and the discrete divergence consistency (DDC) is proposed. The summation of the linear DDC over the whole computational domain leads to the so-called integration constraint in the literature. A three-point integration scheme using background triangle elements is developed, in which the corrected derivatives are computed by the satisfaction of the quadratic DDC. We prove that such smoothed derivatives also meet the quadratic DAC, and therefore, the proposed scheme possesses the quadratic consistency that leads to its name QC3. Numerical results show that QC3 is the only method that can pass both the linear and the quadratic patch tests and achieves the best performances for all the four examples in terms of stability, convergence, accuracy, and efficiency among all the tested methods. Particularly, it shows a huge improvement for the existing linearly consistent one-point integration method in some examples. Copyright © 2012 John Wiley & Sons, Ltd.

Received 13 March 2012; Revised 13 April 2012; Accepted 24 April 2012

KEY WORDS: meshfree; integration; Galerkin; finite element method; elasticity; solids

1. INTRODUCTION

Meshfree Galerkin methods, such as the element-free Galerkin (EFG) method [1], have gained increasing popularity in the literature because they offer substantial potential in many classes of problems, especially those characterized by large deformations. However, their relatively low computational speed still impedes their application in industry. Because of the nonpolynomial character of the meshfree approximation, such as the moving least-squares (MLS), higher-order Gauss quadrature is required than finite element method (FEM), which impairs the computational efficiency of meshfree Galerkin methods.

Several methods were developed in the literature to address this issue. Beissel and Belytschko [2] first present the idea of nodal integration, which integrates the Galerkin weak form only at nodes. The spurious oscillation modes emanating from such insufficient quadrature are removed by least-square stabilization. However, the introduced stabilization term may deteriorate the accuracy and the selection of the stabilization parameter depends on numerical experiments. Chen *et al.* [3,4] proposed a stabilized conforming nodal integration (SCNI) method based on strain smoothing. They showed that the method is stable and more efficient than Gauss quadrature. Another advantage is that

*Correspondence to: Qinglin Duan, Department of Engineering Mechanics, Dalian University of Technology, Dalian, Liaoning 116024, China.

†E-mail: qinglinduan@gmail.com

no stabilization parameter is involved in the method. SCNI has already been successfully used for many problems, for example, the thin-plate analysis by Wang and Chen [5]. However, Puso *et al.* [6] reported that SCNI still could present saw-tooth mode at the domain boundary, and a stabilization term with a tunable parameter is added to further stabilize SCNI. Liu *et al.* [7] developed a nodal integration technique in the framework of meshfree radial point interpolation method, and Taylor's expansion is used for stabilization. However, to make the method stable, the stiffness matrix has to be expanded up to second order, which entails substantial computational expense and also limits its extension to other type of problems. In addition, third-order derivatives of shape functions are required in such stabilization. Bonet and Kulasegaram [8] also studied the nodal integration in smoothed particle hydrodynamics (SPH) methods and proposed their correction and stabilization to make SPH stable and pass the linear patch test.

The spurious modes associated with nodal integration can also be removed or at least be alleviated by using more quadrature points in addition to the nodes. This leads to the so-called stress-point integration method initially developed by Dyka *et al.* [9, 10] for tensile instabilities in SPH. Rabczuk *et al.* [11] showed that using both the approximation nodes and the added stress points as quadrature points results better stability than nodal integration. However, Fries and Belytschko [12] reported that a mild instability still presents, which can result in poor convergence, especially in the case of non-uniform nodal arrangements. To this end, Duan and Belytschko [13] proposed two formulations to further stabilize stress-point integration, that is, the gradient and dilatational stabilizations, which are similar to the least-square stabilization and require experience-dependent numerical parameters.

Another class of methods that should be mentioned is the support integration method that employs integration (evaluation) points over the nodal supports, as proposed by Atluri and Zhu [14] in the meshless local Petrov–Galerkin method and by De and Bathe [15] in the finite sphere method. However, because the integrands of the weak form are evaluated multiple times because of the overlap of the supports and a large number of evaluation points per support are required, these methods are very expensive. Improvements for such support integration method are reported by Kwon *et al.* [16] in the least-squares meshfree method and recently by Liu and Belytschko [17] for dynamic problems.

The purpose of this paper is to develop a robust and efficient integration scheme for meshfree Galerkin methods with quadratic approximations by 'correcting' the nodal derivatives at the quadrature points. The idea of 'correcting' the derivatives is initiated in the context of meshfree methods by Krongauz and Belytschko [18] who proposed the consistent pseudo-derivatives by a linear combination of the derivatives of Shepard functions. They showed that two conditions, that is, the PG1 and PG2 in their paper [18], are required to be met in building the pseudo-derivatives in order to pass the linear patch test and therefore lead to better numerical performance. One is the consistency condition among the derivatives of nodal shape functions imposed by the differentiation of the linear approximation consistency; the other is the condition between a nodal shape function and its derivatives required by the Gauss's theorem (divergence theorem) over the whole computational domain. The latter, or more accurately its discrete version, is also called the integration constraint by Chen *et al.* [3, 4], or recently by Liu and Belytschko [17], the divergence-free condition because of the fact that the integral is zero for any interior node that does not have influence on boundaries. However, because of the inaccuracy of the numerical integrations, the Gauss's theorem, that is, PG2, cannot be satisfied exactly if the quadrature is performed numerically, even if the integrand is integrable. This fact leads to the integration correction by Bonet and Kulasegaram [8] and the SCNI by Chen *et al.* [3, 4].

The strain smoothing technique in SCNI is elegant because it satisfies the integration constraint exactly without any experience-dependant parameters. In essence, its methodology is to build the derivatives of the nodal shape function by the contour integral of the shape function itself. This is also the essential ingredient of the smoothed FEM recently under intensive studies [19–21]. Such idea in finite element field can be traced back to the quasi-conforming elements initiated by Tang *et al.* [22] in 1980 at Dalian University of Technology in China. However, their first paper and the majority of the following papers were in Chinese and published in local journals, except only for a few, which were available in international journals [23, 24].

Note that the two conditions given by Krongauz and Belytschko [18] and the integration constraint [3] as mentioned earlier only deal with the linear approximations, that is, MLS with linear basis. Particularly, the strain smoothing in SCNI [3] is only sufficient for the case of constant strain, which is consistent to the linear approximation for the displacement. In other words, the smoothed (corrected) derivatives in SCNI can only reproduce a constant strain field in each integration cell even if the displacement approximation is quadratic or higher. Therefore, the method is only linearly consistent (LC) and cannot sufficiently exploit the benefit of high-order meshfree approximations.

In this paper, we will develop a robust and efficient integration method with corrected nodal derivatives that are consistent to the quadratic meshfree approximations, that is, they can reproduce a linear strain field in each integration cell. To this end, we extend the previous studies [3, 18] to more general cases and propose a framework for the consistency of the meshfree nodal derivatives, which include the differentiation of the approximation consistency (DAC) and the discrete divergence consistency (DDC). The latter is the discrete form of the divergence theorem between a nodal shape function and its derivatives over the domain of an integration cell. For linear approximations, the summation of the DDC over the whole computational domain leads to the so-called integration constraint [3]. The key contribution of this paper is the proposed three-point integration scheme using background triangle elements, in which the smoothed (corrected) nodal derivatives at quadrature points are computed by the DDC for quadratic approximations, that is, MLS with quadratic basis. We further prove that such corrected nodal derivatives also meet the DAC for quadratic approximations, and therefore, the proposed method is named as quadratically consistent three-point (QC3) integration scheme because it satisfies both the quadratic DAC and the quadratic DDC.

This paper is organized as follows. The EFG method is first reviewed in Section 2. The consistency conditions for the nodal derivatives are studied in Section 3. The proposed integration scheme QC3 is described in Section 4. The quadratic consistency of QC3 is proved in Section 5 followed by the numerical examples in Section 6 and conclusions in Section 7.

2. ELEMENT-FREE GALERKIN METHOD

As one of the main meshfree methods in the literature, the EFG uses the MLS approximation to construct the nodal shape functions. Given a set of nodes \mathbf{X}_I in the domain $\Omega \subset \mathbb{R}^2$, the MLS approximation $u^\rho(\mathbf{x})$ for a scalar function $u(\mathbf{x})$ at an arbitrary point \mathbf{x} in Ω can be written in a form similar to that in FEM,

$$u^\rho(\mathbf{x}) = \sum_I N_I(\mathbf{x}) u_I, \quad (1)$$

where u_I are the nodal parameters and $N_I(\mathbf{x})$ the nodal MLS shape functions, which can be written as

$$N_I(\mathbf{x}) = \mathbf{p}^T(\mathbf{X}_I) w_I(\mathbf{x}) \boldsymbol{\alpha}(\mathbf{x}), \quad (2)$$

where $w_I(\mathbf{x})$ is a weight function that, in this study, has the form

$$w_I(\mathbf{x}) = w(\bar{s}) = \begin{cases} 1.0 - 6\bar{s}^2 + 8\bar{s}^3 - 3\bar{s}^4 & \text{for } \bar{s} \leq 1 \\ 0 & \text{for } \bar{s} > 1, \end{cases} \quad (3)$$

where $\bar{s} = s/r$, r is the radius of the support and $s = |\mathbf{x} - \mathbf{X}_I|$ the distance from the sampling point \mathbf{x} to the node \mathbf{X}_I . $\mathbf{p}(\mathbf{x})$ in Equation (2) is a vector of base functions, which usually includes a complete basis of the polynomials with a given order. The unknown vector $\boldsymbol{\alpha}(\mathbf{x})$ in Equation (2) is computed by the reproducibility condition that requires that the MLS approximation defined in Equation (1) reproduce exactly the polynomial basis $\mathbf{p}(\mathbf{x})$, that is,

$$\mathbf{p}(\mathbf{x}) = \sum_I \mathbf{p}(\mathbf{X}_I) N_I(\mathbf{x}). \quad (4)$$

Substitution of Equation (2) into Equation (4) gives

$$\mathbf{A}(\mathbf{x}) \boldsymbol{\alpha}(\mathbf{x}) = \mathbf{p}(\mathbf{x}), \quad (5)$$

where

$$\mathbf{A}(\mathbf{x}) = \sum_I \mathbf{p}(\mathbf{X}_I) \mathbf{p}^T(\mathbf{X}_I) w_I(\mathbf{x}). \quad (6)$$

Thus, the nodal MLS shape functions $N_I(\mathbf{x})$ can be computed by Equation (2) after solving Equation (5) for the unknown vector $\boldsymbol{\alpha}(\mathbf{x})$.

Traditionally, the derivatives of the shape function $N_{I,i}(\mathbf{x})$ are computed by directly differentiating Equation (2)

$$N_{I,i}(\mathbf{x}) = \mathbf{p}^T(\mathbf{X}_I) [w_{I,i}(\mathbf{x}) \boldsymbol{\alpha}(\mathbf{x}) + w_I(\mathbf{x}) \boldsymbol{\alpha}_{,i}(\mathbf{x})], \quad (7)$$

where the unknown $\boldsymbol{\alpha}_{,i}(\mathbf{x})$ is obtained by directly differentiating Equation (5)

$$\mathbf{A}(\mathbf{x}) \boldsymbol{\alpha}_{,i}(\mathbf{x}) = \mathbf{p}_{,i}(\mathbf{x}) - \mathbf{A}_{,i}(\mathbf{x}) \boldsymbol{\alpha}(\mathbf{x}) \quad (8)$$

with

$$\mathbf{A}_{,i}(\mathbf{x}) = \sum_I \mathbf{p}(\mathbf{X}_I) \mathbf{p}^T(\mathbf{X}_I) w_{I,i}(\mathbf{x}). \quad (9)$$

We now consider an elastostatic boundary value problem on a two-dimensional domain Ω bounded by Γ . The equilibrium equation is

$$\nabla \cdot \boldsymbol{\sigma}(\mathbf{u}) + \mathbf{b} = 0 \text{ in } \Omega, \quad (10)$$

where $\boldsymbol{\sigma}$ is the Cauchy stress tensor and \mathbf{b} the body force vector. The boundary conditions are

$$\boldsymbol{\sigma} \cdot \mathbf{n} = \bar{\mathbf{t}} \text{ on } \Gamma_t, \quad (11)$$

$$\mathbf{u} = \bar{\mathbf{u}} \text{ on } \Gamma_u, \quad (12)$$

where \mathbf{n} is the unit normal to the boundary, and $\bar{\mathbf{t}}$ and $\bar{\mathbf{u}}$ are, respectively, the prescribed traction and displacement on boundaries Γ_t and Γ_u . Note that we have $\Gamma_t \cup \Gamma_u = \Gamma$ and $\Gamma_t \cap \Gamma_u = \emptyset$.

By using the standard Galerkin procedure with Nitsche's method [25] enforcing the essential boundary condition, the final discretized equation is

$$(\mathbf{K} - \mathbf{K}^{\Gamma_u} + \beta \mathbf{K}^p) \mathbf{d} = \mathbf{f} - \mathbf{f}^{\Gamma_u} + \beta \mathbf{f}^p, \quad (13)$$

where

$$\mathbf{K} = \int_{\Omega} \mathbf{B}^T \mathbf{D} \mathbf{B} d\Omega \quad \mathbf{f} = \int_{\Omega} \mathbf{N}^T \mathbf{b} d\Omega + \int_{\Gamma_t} \mathbf{N}^T \bar{\mathbf{t}} d\Gamma \quad \mathbf{B} = \mathcal{L} \mathbf{N}, \quad (14)$$

$$\mathbf{K}^{\Gamma_u} = \int_{\Gamma_u} \left[\mathbf{N}^T (\mathcal{L}_n^T \mathbf{D} \mathcal{L} \mathbf{N}) + (\mathcal{L}_n^T \mathbf{D} \mathcal{L} \mathbf{N})^T \mathbf{N} \right] d\Gamma \quad \mathbf{f}^{\Gamma_u} = \int_{\Gamma_u} (\mathcal{L}_n^T \mathbf{D} \mathcal{L} \mathbf{N})^T \bar{\mathbf{u}} d\Gamma, \quad (15)$$

$$\mathbf{K}^p = \int_{\Gamma_u} \mathbf{N}^T \mathbf{N} d\Gamma \quad \mathbf{f}^p = \int_{\Gamma_u} \mathbf{N}^T \bar{\mathbf{u}} d\Gamma, \quad (16)$$

with

$$\mathcal{L} = \begin{bmatrix} \partial/\partial x & 0 & \partial/\partial y \\ 0 & \partial/\partial y & \partial/\partial x \end{bmatrix}^T \quad \mathcal{L}_n = \begin{bmatrix} n_x & 0 & n_y \\ 0 & n_y & n_x \end{bmatrix}^T. \quad (17)$$

3. CONSISTENCY OF THE NODAL DERIVATIVES

Traditionally, the consistency requirement for the nodal derivatives in meshfree Galerkin methods is only derived from the approximation consistency, which, in MLS, is represented by the so-called reproducibility condition, that is, Equation (4). For quadratic approximations, that is, $\mathbf{p}(\mathbf{x}) = [1 \ x \ y \ x^2 \ xy \ y^2]^T$, the expression of the approximation consistency can be developed as

$$\begin{aligned} \sum_I N_I(\mathbf{x}) &= 1 & \sum_I N_I(\mathbf{x}) X_I &= x & \sum_I N_I(\mathbf{x}) Y_I &= y, \\ \sum_I N_I(\mathbf{x}) X_I^2 &= x^2 & \sum_I N_I(\mathbf{x}) X_I Y_I &= xy & \sum_I N_I(\mathbf{x}) Y_I^2 &= y^2, \end{aligned} \quad (18)$$

where the sampling point $\mathbf{x} = [x, y]$. Obviously, the approximation consistency is satisfied by the nodal MLS shape functions $N_I(\mathbf{x})$ because their construction is based on it as shown in Equations (2)–(6).

By taking spatial derivatives of Equation (4), we have

$$\mathbf{p}_{,i}(\mathbf{x}) = \sum_I \mathbf{p}(\mathbf{X}_I) N_{I,i}(\mathbf{x}), \quad (19)$$

which, in the case of $\mathbf{p}(\mathbf{x}) = [1 \ x \ y \ x^2 \ xy \ y^2]^T$, can be expanded as

$$\begin{aligned} \sum_I N_{I,x}(\mathbf{x}) &= 0 & \sum_I N_{I,x}(\mathbf{x}) X_I &= 1 & \sum_I N_{I,x}(\mathbf{x}) Y_I &= 0 \\ \sum_I N_{I,x}(\mathbf{x}) X_I^2 &= 2x & \sum_I N_{I,x}(\mathbf{x}) X_I Y_I &= y & \sum_I N_{I,x}(\mathbf{x}) Y_I^2 &= 0 \end{aligned} \quad (20)$$

for $N_{I,x}(\mathbf{x})$ and

$$\begin{aligned} \sum_I N_{I,y}(\mathbf{x}) &= 0 & \sum_I N_{I,y}(\mathbf{x}) X_I &= 0 & \sum_I N_{I,y}(\mathbf{x}) Y_I &= 1 \\ \sum_I N_{I,y}(\mathbf{x}) X_I^2 &= 0 & \sum_I N_{I,y}(\mathbf{x}) X_I Y_I &= x & \sum_I N_{I,y}(\mathbf{x}) Y_I^2 &= 2y \end{aligned} \quad (21)$$

for $N_{I,y}(\mathbf{x})$. Equation (19) presents a consistency condition that should be met by the derivatives of the nodal shape functions $N_{I,i}(\mathbf{x})$. In this study, it is named the differentiation of the approximation consistency (DAC) for the nodal derivatives. It is easy to validate that the traditional MLS nodal derivatives defined and computed by Equations (7)–(9) meet such consistency requirement if we multiply $\mathbf{p}(\mathbf{X}_I)$ at both sides of Equation (7) and then do the summation over I as

$$\begin{aligned} \sum_I \mathbf{p}(\mathbf{X}_I) N_{I,i}(\mathbf{x}) &= \sum_I \mathbf{p}(\mathbf{X}_I) \mathbf{p}^T(\mathbf{X}_I) [w_{I,i}(\mathbf{x}) \boldsymbol{\alpha}(\mathbf{x}) + w_I(\mathbf{x}) \boldsymbol{\alpha}_{,i}(\mathbf{x})] \\ &= \mathbf{A}_{,i}(\mathbf{x}) \boldsymbol{\alpha}(\mathbf{x}) + \mathbf{A}(\mathbf{x}) \boldsymbol{\alpha}_{,i}(\mathbf{x}) = \mathbf{p}_{,i}(\mathbf{x}). \end{aligned} \quad (22)$$

Equations (6), (8), and (9) are used in the derivation of Equation (22).

It is noted that the DAC given in Equation (19) is a requirement only among $N_{I,i}(\mathbf{x})$, not explicitly related to $N_I(\mathbf{x})$. However, each nodal MLS shape function $N_I(\mathbf{x})$, as a smooth function, also has a consistency condition to be met with its derivatives $N_{I,i}(\mathbf{x})$ in terms of the divergence theorem. Such *divergence consistency* (DC) can be expressed as

$$\int_{\Omega_S} N_{I,i}(\mathbf{x}) f(\mathbf{x}) d\Omega = \int_{\Gamma_S} N_I(\mathbf{x}) f(\mathbf{x}) n_i d\Gamma - \int_{\Omega_S} N_I(\mathbf{x}) f_{,i}(\mathbf{x}) d\Omega, \quad (23)$$

where Ω_S bounded by Γ_S is a subdomain where $N_I(\mathbf{x})$ has an influence. Theoretically, Equation (23) should be met by $N_I(\mathbf{x})$ and $N_{I,i}(\mathbf{x})$ for any smooth function $f(\mathbf{x})$. However, in

practice, such rigorous condition cannot be reached, and it is necessary only for some smooth function $f(\mathbf{x})$ closely related to the problem under study. For the elastostatic problem of this study, the set of key functions $f(\mathbf{x})$ can be determined by an analysis of the integration by parts we use in the derivation of the weak form from the equilibrium equation (strong form),

$$\int_{\Omega} N_I(\mathbf{x}) \sigma_{ij,j}(\mathbf{x}) d\Omega = \int_{\Gamma} N_I(\mathbf{x}) \sigma_{ij}(\mathbf{x}) n_j d\Gamma - \int_{\Omega} N_{I,j}(\mathbf{x}) \sigma_{ij}(\mathbf{x}) d\Omega, \quad (24)$$

where Ω bounded by Γ is the whole solution domain. It is noted that the relation also applies to the subdomains Ω_S represented by the background integration cells, that is,

$$\int_{\Omega_S} N_I(\mathbf{x}) \sigma_{ij,j}(\mathbf{x}) d\Omega = \int_{\Gamma_S} N_I(\mathbf{x}) \sigma_{ij}(\mathbf{x}) n_j d\Gamma - \int_{\Omega_S} N_{I,j}(\mathbf{x}) \sigma_{ij}(\mathbf{x}) d\Omega. \quad (25)$$

If we use the quadratic basis $\mathbf{p}(\mathbf{x}) = [1 \ x \ y \ x^2 \ xy \ y^2]^T$ to construct the approximation, that is, the displacement field, the corresponding stress is linear in each Ω_S , that is, $\sigma_{ij}(\mathbf{x}) = a_0 + a_1 x + a_2 y$. Therefore, by comparing Equation (23) with Equation (25), we obtain that the key functions $f(\mathbf{x})$ for elastostatic problem with quadratic approximation for the displacement is the linear basis $[1 \ x \ y]^T$, and then such DC requirement between $N_I(\mathbf{x})$ and $N_{I,i}(\mathbf{x})$ for quadratic approximation can be expanded as

$$\begin{aligned} \int_{\Omega_S} N_{I,x}(\mathbf{x}) d\Omega &= \int_{\Gamma_S} N_I(\mathbf{x}) n_x d\Gamma \\ \int_{\Omega_S} N_{I,x}(\mathbf{x}) x d\Omega &= \int_{\Gamma_S} N_I(\mathbf{x}) x n_x d\Gamma - \int_{\Omega_S} N_I(\mathbf{x}) d\Omega \\ \int_{\Omega_S} N_{I,x}(\mathbf{x}) y d\Omega &= \int_{\Gamma_S} N_I(\mathbf{x}) y n_x d\Gamma \end{aligned} \quad (26)$$

for $N_{I,x}(\mathbf{x})$ and

$$\begin{aligned} \int_{\Omega_S} N_{I,y}(\mathbf{x}) d\Omega &= \int_{\Gamma_S} N_I(\mathbf{x}) n_y d\Gamma \\ \int_{\Omega_S} N_{I,y}(\mathbf{x}) x d\Omega &= \int_{\Gamma_S} N_I(\mathbf{x}) x n_y d\Gamma \\ \int_{\Omega_S} N_{I,y}(\mathbf{x}) y d\Omega &= \int_{\Gamma_S} N_I(\mathbf{x}) y n_y d\Gamma - \int_{\Omega_S} N_I(\mathbf{x}) d\Omega \end{aligned} \quad (27)$$

for $N_{I,y}(\mathbf{x})$. Generally, the proposed DC for elastostatic problem can be formally expressed as follows: If the displacement is approximated by the MLS shape functions $N_I(\mathbf{x})$ with the basis $\mathbf{p}(\mathbf{x})$, the derivatives of the shape functions $N_{I,i}(\mathbf{x})$ must meet the following condition in terms of the basis $\mathbf{q}(\mathbf{x}) = \mathbf{p}_{,x}(\mathbf{x}) \cup \mathbf{p}_{,y}(\mathbf{x})$ for any background integration cell Ω_S where $N_I(\mathbf{x})$ has an influence,

$$\int_{\Omega_S} N_{I,i}(\mathbf{x}) \mathbf{q}(\mathbf{x}) d\Omega = \int_{\Gamma_S} N_I(\mathbf{x}) \mathbf{q}(\mathbf{x}) n_i d\Gamma - \int_{\Omega_S} N_I(\mathbf{x}) \mathbf{q}_{,i}(\mathbf{x}) d\Omega. \quad (28)$$

Obviously, for the quadratic basis $\mathbf{p}(\mathbf{x}) = [1 \ x \ y \ x^2 \ xy \ y^2]^T$, we have $\mathbf{q}(\mathbf{x}) = \mathbf{p}_{,x}(\mathbf{x}) \cup \mathbf{p}_{,y}(\mathbf{x}) = [1 \ x \ y]^T$.

Note that the integration in Equation (28) is on subcells Ω_S , not on the whole domain Ω . In the case of linear approximation, that is, $\mathbf{p}(\mathbf{x}) = [1 \ x \ y]^T$ and $\mathbf{q}(\mathbf{x}) = [1]$, the summation of Equation (28) for all the background integration cells leads to the PG2 condition in [18], that is,

$$\int_{\Omega} N_{I,i}(\mathbf{x}) d\Omega = \int_{\Gamma} N_I(\mathbf{x}) n_i d\Gamma. \quad (29)$$

After the integration is computed numerically, the discrete version of Equation (28) is written as

$$\sum_{H=1}^{m_H} W_H N_{I,i}(\mathbf{x}_H) \mathbf{q}(\mathbf{x}_H) = \sum_{L=1}^{K_L} \sum_{G=1}^{m_G} N_I(\mathbf{x}_G) \mathbf{q}(\mathbf{x}_G) n_i^L w_G - \sum_{H=1}^{m_H} W_H N_I(\mathbf{x}_H) \mathbf{q}_{,i}(\mathbf{x}_H), \quad (30)$$

where m_H is the number of integration points per cell Ω_S , K_L the number of edges of Ω_S , m_G the number of integration points per edge, and W_H and w_G the integration weights for domain and boundary integrations, respectively. To be more exact, the nodal shape function $N_I(\mathbf{x})$ and its derivatives $N_{I,i}(\mathbf{x})$ should meet Equation (30) instead of Equation (28) because all the quadratures are numerically computed in meshfree Galerkin method. Equation (30) is called the discrete divergence consistency (DDC) for the nodal derivatives.

Note that the DDC given in Equation (30) generalizes the so-called integration constraint in [3] to any basis $\mathbf{p}(\mathbf{x})$, and an additional domain integration term presents on the right-hand side of Equation (30) because of this generalization. For linear approximation with $\mathbf{p}(\mathbf{x}) = [1 \ x \ y]^T$ and $\mathbf{q}(\mathbf{x}) = [1]$, the summation of Equation (30) for all the background integration cells leads to the so-called integration constraint in [3], that is,

$$\sum_{H=1}^{T_H} W_H N_{I,i}(\mathbf{x}_H) = \sum_{L=1}^{T_L} \sum_{G=1}^{m_G} N_I(\mathbf{x}_G) n_i^L w_G, \quad (31)$$

where T_H is the total number of integration points in the whole domain Ω and T_L the total number of edges to discretize the whole boundary Γ . We note that, here, $\Gamma = \Gamma_t \cup \Gamma_u$, that is, includes both essential and natural boundaries. As pointed out in [3, 18], for interior nodes that have no influence on the boundaries, the right-hand side of Equation (31) is zero. Because we formulate this condition directly on the background integration cells, not on the whole domain as given by Krongauz and Belytschko [18] and Chen *et al.* [3], we do not need to treat the interior and boundary nodes differently.

In summary, both the DAC and DDC should be met. Therefore, the proposed consistency framework for the nodal derivatives can be formally expressed as follows: If the displacement is approximated by the MLS shape functions $N_I(\mathbf{x})$ with the basis $\mathbf{p}(\mathbf{x})$, the derivatives of the shape functions $N_{I,i}(\mathbf{x})$ must meet the DAC given in Equation (19) and the DDC given by Equation (30) with $\mathbf{q}(\mathbf{x}) = \mathbf{p}_{,x}(\mathbf{x}) \cup \mathbf{p}_{,y}(\mathbf{x})$.

4. QUADRATICALLY CONSISTENT THREE-POINT INTEGRATION SCHEME

As mentioned earlier, the traditional nodal MLS derivatives computed in Equations (7)–(9) only meet the DAC, that is, Equation (19), whereas the DDC is not satisfied. Here, we propose a scheme to compute the MLS derivatives for quadratic approximations, which is based on a direct satisfaction of the quadratic DDC, that is, Equation (30) with $\mathbf{q}(\mathbf{x}) = [1 \ x \ y]^T$. The proposed scheme uses three quadrature points in each background triangle element. We can prove in the next section that such scheme also meets the quadratic DAC, that is, Equation (19) with $\mathbf{p}(\mathbf{x}) = [1 \ x \ y \ x^2 \ xy \ y^2]^T$ and expanded as Equations (20)–(21). Hence, we name it the QC3 integration scheme.

As shown in Figure 1, the dark dots are the nodes that are used to construct the mesh-free approximation. The symbol orange triangles denote the vertices of the background triangle mesh for the domain integration. In each background triangle element, we use three quadrature points, denoted by red crosses, for the domain integration. They have the same integration weight, that is, $1/3$ for each point, and their triangular (area) coordinates are respectively, $(2/3, 1/6, 1/6)$, $(1/6, 2/3, 1/6)$, $(1/6, 1/6, 2/3)$ [26]. The blue stars on the edges of the background triangles are the one-dimensional Gauss points for boundary integrations.

Let the subdomain Ω_S bounded by Γ_S be the background triangle element under consideration and Γ_S the three edges of the element; \mathbf{x}_H and W_H be the location and weights, respectively, of

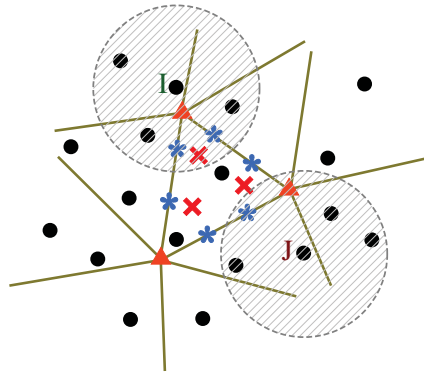


Figure 1. Schematic diagram of the quadratically consistent three-point integration scheme.

the three evaluation points ($H = 1 \sim 3$) in Ω_S ; and \mathbf{x}_G and w_G be the location and weights, respectively, of the two Gauss points ($G = 1 \sim 2$) on edges Γ_L . We have $\bigcup_{L=1}^3 \Gamma_L = \Gamma_S$.

For node I whose nodal shape function $N_I(\mathbf{x})$ has an influence in Ω_S , its x -derivatives at the three evaluation points, that is, $N_{I,x}(\mathbf{x}_H)$, can be computed by solving the quadratic DDC for $N_{I,x}(\mathbf{x})$, that is, the discrete version of Equation (26),

$$\begin{aligned} W_1 N_{I,x}(\mathbf{x}_1) + W_2 N_{I,x}(\mathbf{x}_2) + W_3 N_{I,x}(\mathbf{x}_3) &= \sum_{L=1}^3 \sum_{G=1}^2 N_I(\mathbf{x}_G) n_x^L w_G, \\ W_1 x_1 N_{I,x}(\mathbf{x}_1) + W_2 x_2 N_{I,x}(\mathbf{x}_2) + W_3 x_3 N_{I,x}(\mathbf{x}_3) &= \sum_{L=1}^3 \sum_{G=1}^2 N_I(\mathbf{x}_G) x_G n_x^L w_G - \sum_{H=1}^3 W_H N_I(\mathbf{x}_H), \\ W_1 y_1 N_{I,x}(\mathbf{x}_1) + W_2 y_2 N_{I,x}(\mathbf{x}_2) + W_3 y_3 N_{I,x}(\mathbf{x}_3) &= \sum_{L=1}^3 \sum_{G=1}^2 N_I(\mathbf{x}_G) y_G n_x^L w_G, \end{aligned}$$

which can be written in a matrix–vector format as

$$\mathbf{W} \mathbf{d}_x = \mathbf{f}_x, \quad (32)$$

where

$$\mathbf{W} = \begin{bmatrix} W_1 & W_2 & W_3 \\ W_1 x_1 & W_2 x_2 & W_3 x_3 \\ W_1 y_1 & W_2 y_2 & W_3 y_3 \end{bmatrix}, \quad \mathbf{d}_x = \begin{Bmatrix} N_{I,x}(\mathbf{x}_1) \\ N_{I,x}(\mathbf{x}_2) \\ N_{I,x}(\mathbf{x}_3) \end{Bmatrix}, \quad (33)$$

$$\mathbf{f}_x = \begin{Bmatrix} \sum_{L=1}^3 \sum_{G=1}^2 N_I(\mathbf{x}_G) n_x^L w_G \\ \sum_{L=1}^3 \sum_{G=1}^2 N_I(\mathbf{x}_G) x_G n_x^L w_G - \sum_{H=1}^3 W_H N_I(\mathbf{x}_H) \\ \sum_{L=1}^3 \sum_{G=1}^2 N_I(\mathbf{x}_G) y_G n_x^L w_G \end{Bmatrix}. \quad (34)$$

With the specified three evaluation points in the triangle element, two Gauss points per edge, and the standard nodal MLS shape functions $N_I(\mathbf{x})$, the matrix \mathbf{W} and the vector \mathbf{f}_x are computable. By solving Equation (32), we can obtain the corrected (smoothed) nodal derivatives at the three integration points.

Note that the influence of $N_I(\mathbf{x})$ to the subcell Ω_S is determined by the boundary quadrature points, that is, the blue stars in Figure 1. In other words, a node will have its influence to an integration cell provided that its MLS influence domain covers some Gauss points on the cell boundary, even if no evaluation points of the cell is inside its influence domain, as the node J in Figure 1 (shaded area denotes the nodal influence domain).

The regularity of the matrix \mathbf{W} is very important to the proposed method because it determines the existence of the solution to Equation (32), that is, the existence of such smoothed (corrected) nodal derivatives. The three quadrature points have the same weight, that is, $W_1 = W_2 = W_3 = W$, and the matrix \mathbf{W} can be written as

$$\mathbf{W} = W \begin{bmatrix} 1 & 1 & 1 \\ x_1 & x_2 & x_3 \\ y_1 & y_2 & y_3 \end{bmatrix}. \quad (35)$$

Obviously, the matrix \mathbf{W} as shown in Equation (35) is full rank provided that the three evaluation points are not collinear. This leads to the regularity of \mathbf{W} , that is, Equation (32) always has one unique solution. This is an important property of the proposed method because it guarantees the existence and the uniqueness of the smoothed nodal derivatives provided that the background triangles do not degenerate to lines.

In the same way, the smoothed derivative with respect to y , that is, $\mathbf{d}_y = \{N_{I,y}(\mathbf{x}_1) \ N_{I,y}(\mathbf{x}_2) \ N_{I,y}(\mathbf{x}_3)\}^T$, can also be obtained by solving the discrete version of Equation (27). Note that the matrix \mathbf{W} is not symmetric and it is the same for the solution of \mathbf{d}_x and \mathbf{d}_y . Therefore, it can be factored and stored to accelerate the computation.

It is noted that we use three points per cell to enforce the quadratic DDC, which includes three equations as shown in Equation (30) with $\mathbf{q}(\mathbf{x}) = [1 \ x \ y]^T$. If only one quadrature point per cell at the cell center is used, like SCNI [3], then only the linear DDC, that is, Equation (30) with $\mathbf{q}(\mathbf{x}) = [1]$, can be enforced and Equation (32) reduces to the one equation as follows:

$$AN_{I,x}(\mathbf{x}_c) = \sum_{L=1}^3 \sum_{G=1}^2 N_I(\mathbf{x}_G) n_x^L w_G, \quad (36)$$

where A is the area of the cell and \mathbf{x}_c is its center. This is essentially the equation employed in SCNI [3] to compute the smoothed strain. The difference is that Voronoi diagram is used there and quadrature points coincide with the nodes. Such one-point integration can only reproduce a constant strain field, that is, the smoothed nodal derivatives computed in Equation (36) are constant in each integration cell. In contrast, by using three points per cell in the proposed QC3 scheme, the corrected derivatives solved in Equation (32) are able to represent a linear field, that is, they can reproduce a linear strain field.

5. THE QUADRATIC CONSISTENCY OF THE QC3

To show that the proposed scheme QC3 is quadratically consistent (QC) for MLS approximations with $\mathbf{p}(\mathbf{x}) = [1 \ x \ y \ x^2 \ xy \ y^2]^T$, we must prove that both the quadratic DAC and the quadratic DDC for the nodal derivatives are met by this scheme. Obviously, the latter is met because the computation of the nodal derivatives is directly based on the satisfaction of such consistency, as described in the last section. However, whether the quadratic DAC, that is, Equation (20) for $N_{I,x}(\mathbf{x})$ and Equation (21) for $N_{I,y}(\mathbf{x})$, is met or not is still unknown. In the following, we will give such proof.

Before proceeding with the proof, we introduce the following expression:

$$\begin{aligned} \mathbf{p}(\mathbf{x}) &= [1 \ x \ y \ x^2 \ xy \ y^2]^T \\ &= [p_1(\mathbf{x}) \ p_2(\mathbf{x}) \ p_3(\mathbf{x}) \ p_4(\mathbf{x}) \ p_5(\mathbf{x}) \ p_6(\mathbf{x})]^T, \end{aligned} \quad (37)$$

and we have

$$\begin{aligned} \mathbf{p}(\mathbf{X}_I) &= [1 \quad X_I \quad Y_I \quad X_I^2 \quad X_I Y_I \quad Y_I^2]^T \\ &= [p_1(\mathbf{X}_I) \quad p_2(\mathbf{X}_I) \quad p_3(\mathbf{X}_I) \quad p_4(\mathbf{X}_I) \quad p_5(\mathbf{X}_I) \quad p_6(\mathbf{X}_I)]^T, \end{aligned} \quad (38)$$

such that the quadratic DAC for $N_{I,x}(\mathbf{x})$, that is, Equation (20), can be written in a concise form as

$$\sum_I N_{I,x}(\mathbf{x}) p_j(\mathbf{X}_I) = p_{j,x}(\mathbf{x}) \quad (j = 1 \sim 6). \quad (39)$$

To prove that Equation (39) holds at the three quadrature points $\mathbf{x}_H (H = 1 \sim 3)$, we multiply $p_j(\mathbf{X}_I)$ at both sides of Equation (32) and then do the summation over I , that is,

$$\mathbf{W} \sum_I \mathbf{d}_x p_j(\mathbf{X}_I) = \sum_I \mathbf{f}_x p_j(\mathbf{X}_I), \quad (40)$$

where the right-hand side

$$\begin{aligned} \sum_I \mathbf{f}_x p_j(\mathbf{X}_I) &= \left\{ \begin{aligned} &\sum_{L=1}^3 \sum_{G=1}^2 \sum_I N_I(\mathbf{x}_G) p_j(\mathbf{X}_I) n_x^L w_G \\ &\sum_{L=1}^3 \sum_{G=1}^2 \sum_I N_I(\mathbf{x}_G) p_j(\mathbf{X}_I) x_G n_x^L w_G - \sum_{H=1}^3 \sum_I N_I(\mathbf{x}_H) p_j(\mathbf{X}_I) W_H \\ &\sum_{L=1}^3 \sum_{G=1}^2 \sum_I N_I(\mathbf{x}_G) p_j(\mathbf{X}_I) y_G n_x^L w_G \end{aligned} \right\} \\ &= \left\{ \begin{aligned} &\sum_{L=1}^3 \sum_{G=1}^2 p_j(\mathbf{x}_G) n_x^L w_G \\ &\sum_{L=1}^3 \sum_{G=1}^2 p_j(\mathbf{x}_G) x_G n_x^L w_G - \sum_{H=1}^3 p_j(\mathbf{x}_H) W_H \\ &\sum_{L=1}^3 \sum_{G=1}^2 p_j(\mathbf{x}_G) y_G n_x^L w_G \end{aligned} \right\} \\ &= \left\{ \begin{aligned} &\int_{\Gamma_S} p_j(\mathbf{x}) n_x d\Gamma \\ &\int_{\Gamma_S} p_j(\mathbf{x}) x n_x d\Gamma - \int_{\Omega_S} p_j(\mathbf{x}) d\Omega \\ &\int_{\Gamma_S} p_j(\mathbf{x}) y n_x d\Gamma \end{aligned} \right\} = \left\{ \begin{aligned} &\int_{\Omega_S} p_{j,x}(\mathbf{x}) d\Omega \\ &\int_{\Omega_S} p_{j,x}(\mathbf{x}) x d\Omega \\ &\int_{\Omega_S} p_{j,x}(\mathbf{x}) y d\Omega \end{aligned} \right\} \\ &= \left\{ \begin{aligned} &W_1 p_{j,x}(\mathbf{x}_1) + W_2 p_{j,x}(\mathbf{x}_2) + W_3 p_{j,x}(\mathbf{x}_3) \\ &W_1 x_1 p_{j,x}(\mathbf{x}_1) + W_2 x_2 p_{j,x}(\mathbf{x}_2) + W_3 x_3 p_{j,x}(\mathbf{x}_3) \\ &W_1 y_1 p_{j,x}(\mathbf{x}_1) + W_2 y_2 p_{j,x}(\mathbf{x}_2) + W_3 y_3 p_{j,x}(\mathbf{x}_3) \end{aligned} \right\}. \quad (41)$$

The second equal sign is due to the approximation consistency, that is, Equation (18), which also can be written as

$$\sum_I N_I(\mathbf{x}) p_j(\mathbf{X}_I) = p_j(\mathbf{x}) \quad (j = 1 \sim 6). \quad (42)$$

The fourth equal sign in Equation (41) is due to the divergence theorem. Note that we use three evaluation points per cell for domain integration and two Gauss points per edge for boundary integration, thus up to second-order polynomial over the cell domain and up to third-order polynomial along the edges can be integrated exactly. This property guarantees the conversion between the discrete summation and the continuous integral in Equation (41), that is, the third and the last equal signs. Substitution of Equations (33) and (41) into Equation (40) gives

$$\begin{aligned}
& \begin{bmatrix} W_1 & W_2 & W_3 \\ W_1 x_1 & W_2 x_2 & W_3 x_3 \\ W_1 y_1 & W_2 y_2 & W_3 y_3 \end{bmatrix} \begin{Bmatrix} \sum_I N_{I,x}(\mathbf{x}_1) p_j(\mathbf{X}_I) \\ \sum_I N_{I,x}(\mathbf{x}_2) p_j(\mathbf{X}_I) \\ \sum_I N_{I,x}(\mathbf{x}_3) p_j(\mathbf{X}_I) \end{Bmatrix} \\
&= \begin{Bmatrix} W_1 p_{j,x}(\mathbf{x}_1) + W_2 p_{j,x}(\mathbf{x}_2) + W_3 p_{j,x}(\mathbf{x}_3) \\ W_1 x_1 p_{j,x}(\mathbf{x}_1) + W_2 x_2 p_{j,x}(\mathbf{x}_2) + W_3 x_3 p_{j,x}(\mathbf{x}_3) \\ W_1 y_1 p_{j,x}(\mathbf{x}_1) + W_2 y_2 p_{j,x}(\mathbf{x}_2) + W_3 y_3 p_{j,x}(\mathbf{x}_3) \end{Bmatrix}.
\end{aligned} \quad (43)$$

The regularity of the matrix \mathbf{W} guarantees that Equation (43) has the only one solution

$$\sum_I N_{I,x}(\mathbf{x}_H) p_j(\mathbf{X}_I) = p_{j,x}(\mathbf{x}_H) \quad (j = 1 \sim 6, H = 1 \sim 3), \quad (44)$$

which completes our proof. In the same way, the quadratic DAC for $N_{I,y}(\mathbf{x})$, that is, Equation (21), can also be easily proved.

Thus, we reach the following statement: If the approximation possesses second-order consistency, that is, meets Equation (18), the proposed scheme QC3 meets both the quadratic DAC, that is, Equations (20) and (21), and the quadratic DDC, that is, Equation (30) with $\mathbf{q}(\mathbf{x}) = [1 \ x \ y]^T$. Therefore, it is quadratically consistent, which leads to its name QC3.

As discussed in the last section, if only one quadrature point per cell at the cell center is used, like SCNI [3], then only linear DDC, that is, Equation (30) with $\mathbf{q}(\mathbf{x}) = [1]$, can be enforced even if the approximation is quadratic. However, in this case, the smoothed nodal derivatives computed in Equation (36) still meet the quadratic DAC, that is, Equation (39). This can be easily proved if we multiply $p_j(\mathbf{X}_I)$ at both sides of Equation (36) and then do the summation over I as follows:

$$\begin{aligned}
\sum_I N_{I,x}(\mathbf{x}_c) p_j(\mathbf{X}_I) &= \frac{1}{A} \sum_{L=1}^3 \sum_{G=1}^2 \sum_I N_I(\mathbf{x}_G) p_j(\mathbf{X}_I) n_x^L w_G = \frac{1}{A} \sum_{L=1}^3 \sum_{G=1}^2 p_j(\mathbf{x}_G) n_x^L w_G \\
&= \frac{1}{A} \int_{\Gamma_S} p_j(\mathbf{x}) n_x d\Gamma = \frac{1}{A} \int_{\Omega_S} p_{j,x}(\mathbf{x}) d\Omega = p_{j,x}(\mathbf{x}_c).
\end{aligned} \quad (45)$$

The last equal sign is due to the fact that a linear function over the cell Ω_S can be exactly integrated by using only its center \mathbf{x}_c . In Equation (45), we can see that such one-point integration meets the quadratic DAC provided that the MLS shape functions are constructed with a quadratic basis and two Gauss points are used for boundary integrations. This property should also apply to SCNI [3]. Such proof is not given in [3], but instead, the strain smoothing technique is used there.

It is noted that, although this one-point integration scheme meets the quadratic DAC for nodal derivatives, the quadratic DDC is not met. Therefore, it is still only LC because both the linear DDC and the linear DAC for derivatives are met by this scheme. This method is called *linearly consistent one-point (LC1)* integration scheme in this study, which corresponds to SCNI [3]. In the next section, we will show that, because of its lack of the satisfaction of the quadratic DDC, LC1 only achieves a similar numerical performance as the linear finite element method (LFEM) even if the MLS approximation is quadratic.

6. NUMERICAL EXAMPLES

The following five examples are presented in this section. The material parameters for all the examples are $E = 10^7 \text{Pa}$, $\nu = 0.3$, and plane stress conditions are assumed. The normalized L_2 norm of the displacement and the energy errors are respectively defined as

$$E^{\text{disp}} = \left[\frac{\sum_I^n (\mathbf{u}_I^h - \mathbf{u}_I^e)^T (\mathbf{u}_I^h - \mathbf{u}_I^e)}{\sum_I^n \mathbf{u}_I^{eT} \mathbf{u}_I^e} \right]^{\frac{1}{2}}, \quad E^{\text{eng}} = \left[\frac{\int_{\Omega} (\boldsymbol{\varepsilon}^h - \boldsymbol{\varepsilon}^e)^T \mathbf{D} (\boldsymbol{\varepsilon}^h - \boldsymbol{\varepsilon}^e) d\Omega}{\int_{\Omega} \boldsymbol{\varepsilon}^{eT} \mathbf{D} \boldsymbol{\varepsilon}^e d\Omega} \right]^{\frac{1}{2}}, \quad (46)$$

where the superscripts e and h denote the exact and the numerical solutions, respectively.

The quadratic basis $\mathbf{p}(\mathbf{x}) = [1 \ x \ y \ x^2 \ xy \ y^2]^T$ is used in MLS approximation, and the radius of the support for node I is

$$r_I = ch_I^{\max} \quad (47)$$

with $c = 2.5$, and h_I^{\max} is computed by

$$h_I^{\max} = \max_{J \in S_I} \|\mathbf{X}_I - \mathbf{X}_J\|, \quad (48)$$

where S_I is the set of neighboring points of node I that constructs a polygon surrounding node I . The essential boundary conditions are enforced by the Nitsche's method with $\beta = 10^5 E$.

Solutions are reported for the EFG method with the developed QC3 scheme, the LC1 scheme, and the *standard triangle* (ST) integration scheme with 1, 3, 7, and 16 quadrature points, respectively. The latter is denoted as ST1, ST3, ST7, and ST16, respectively. Note that the traditional derivatives of the MLS shape functions defined by Equations (7)–(9) are used in the ST schemes. The results by the LFEM are also provided. For all the methods, the energy error E^{eng} in Equation (46) are evaluated by 16 quadrature points in each background triangle element, that is, by the ST16 scheme.

6.1. Patch tests

Patch test is first investigated on a 2×2 domain with 5×5 nodes. Both regular and irregular arrangements of the nodes are tested. The irregular configuration of the nodes is generated by a perturbation to the location of the interior nodes in regular configuration as

$$x_{\text{ir}} = x_{\text{r}} + (-1)^{i_x} c_x h \quad y_{\text{ir}} = y_{\text{r}} + (-1)^{i_y} c_y h, \quad (49)$$

where the subscripts ir and r denote irregular and regular configurations, respectively; i_x and i_y are two random integers; c_x and c_y the perturbation parameters; and $h = 0.5$ the 'mesh' size or the typical size of the discretization. In this study, we choose $c_x = c_y = 0.15$.

6.1.1. Linear patch For the linear patch test, all the boundary displacements are prescribed as

$$\bar{\mathbf{u}} = \left\{ \begin{array}{l} 0.1 + 0.1x + 0.2y \\ 0.05 + 0.15x + 0.1y \end{array} \right\}. \quad (50)$$

The exact solution is $\mathbf{u} = \bar{\mathbf{u}}$ in the absence of body forces. Tables I and II show the errors in displacement and energy computed in Equation (46) for all the tested methods by using regular and irregular nodal configurations, respectively.

The developed QC3, LC1, and LFEM passed the linear patch tests for both regular and irregular nodal configurations because their errors in both displacement and energy are less than 1×10^{-10} .

Table I. Linear patch test in regular nodal configuration.

	QC3	LC1	ST1	ST3	ST7	ST16	LFEM
E^{disp}	0.96E-12	0.28E-11	0.47E-03	0.72E-04	0.51E-05	0.12E-05	0.47E-15
E^{eng}	0.90E-11	0.25E-10	0.39E-02	0.59E-03	0.41E-04	0.95E-05	0.21E-14

QC3, quadratically consistent three-point; LC1, linearly consistent one-point; ST, standard triangle; LFEM, linear finite element method.

Table II. Linear patch test in irregular nodal configuration.

	QC3	LC1	ST1	ST3	ST7	ST16	LFEM
E^{disp}	0.31E-12	0.68E-12	0.24E-02	0.17E-03	0.46E-04	0.87E-05	0.28E-15
E^{eng}	0.25E-11	0.49E-11	0.18E-01	0.17E-02	0.44E-03	0.81E-04	0.16E-14

QC3, quadratically consistent three-point; LC1, linearly consistent one-point; ST, standard triangle; LFEM, linear finite element method.

This demonstrates their abilities to reproduce linear displacement field and constant strain field within roundoff errors. It is not a surprise for QC3 and LC1 because they satisfy the linear DAC and DDC, which are the necessary conditions to pass the linear patch test.

The EFG methods using the ST integration schemes exhibit relatively large errors in both displacement and energy, although the errors decrease with increasing number of evaluation points. However, even by using 16 integration points per element, considerable errors on the order of 10^{-6} in displacement and 10^{-5} in energy resulted in comparison with the QC3 scheme whose errors are on the order of 10^{-13} in displacement and 10^{-12} in energy. Although the accuracy on the order of 10^{-6} is enough for general engineering problems, it is still not enough for passing such simple linear patch test exactly in a numerical sense. In other words, 10^{-6} is not within the roundoff errors in this case and the ST schemes fail to pass the test ‘exactly’.

6.1.2. Quadratic patch In quadratic patch test, displacement is prescribed at domain boundaries as

$$\bar{\mathbf{u}} = \begin{Bmatrix} 0.1x^2 + 0.1xy + 0.2y^2 \\ 0.15x^2 + 0.29xy + 0.06y^2 \end{Bmatrix}. \quad (51)$$

The exact solution to this problem is $\mathbf{u} = \bar{\mathbf{u}}$ if the following constant body forces are applied:

$$\mathbf{b} = \begin{Bmatrix} -0.2\mathbf{D}(1, 1) - 0.29\mathbf{D}(1, 2) - 0.4\mathbf{D}(3, 3) \\ -0.12\mathbf{D}(1, 1) - 0.1\mathbf{D}(1, 2) - 0.69\mathbf{D}(3, 3) \end{Bmatrix}, \quad (52)$$

where the matrix \mathbf{D} is the elastic moduli in Equation (14).

The results are shown in Tables III and IV for regular and irregular nodal configurations, respectively. Obviously, only the proposed QC3 scheme passed the quadratic patch test. This is a direct consequence of its satisfaction of both the quadratic DAC and the quadratic DDC.

The LC1 scheme failed even if the quadratic MLS approximation was used. This is not a surprise because the quadratic DDC is not satisfied by this scheme. Note that LC1 corresponds to the SCNI [3], and therefore, this conclusion should also apply to SCNI even if we did not do the integration at nodes, that is, SCNI cannot pass the quadratic patch test.

Table III. Quadratic patch test in regular nodal configuration.

	QC3	LC1	ST1	ST3	ST7	ST16	LFEM
E^{disp}	0.12E-11	0.99E-02	0.16E-01	0.49E-03	0.12E-03	0.10E-03	0.39E-15
E^{eng}	0.62E-11	0.60E-01	0.94E-01	0.25E-02	0.60E-03	0.57E-03	0.11E+00

QC3, quadratically consistent three-point; LC1, linearly consistent one-point; ST, standard triangle; LFEM, linear finite element method.

Table IV. Quadratic patch test in irregular nodal configuration.

	QC3	LC1	ST1	ST3	ST7	ST16	LFEM
E^{disp}	0.83E-12	0.13E-02	0.40E-02	0.24E-03	0.51E-04	0.25E-04	0.19E-02
E^{eng}	0.36E-11	0.99E-02	0.20E-01	0.11E-02	0.29E-03	0.11E-03	0.12E+00

QC3, quadratically consistent three-point; LC1, linearly consistent one-point; ST, standard triangle; LFEM, linear finite element method.

The ST schemes resulted even larger errors than what they did in the linear patch test and failed to pass the test without doubt. It is surprising that LFEM can reproduce the quadratic displacement field exactly with a regular mesh because its error in displacement is on the order of 10^{-15} , as shown in Table III. This is probably because the regular mesh provides some sort of ‘symmetry’. However, it resulted large errors in energy. For irregular mesh, both the displacement and energy errors of the LFEM are not acceptable. Therefore, LFEM failed to pass the quadratic patch test.

The patch tests in this study show that the traditional integration method for triangles, referred to as the ST integration, cannot make the EFG method pass the linear and quadratic patch tests provided a rigorous threshold is applied to the numerical roundoff errors, for example, the order of 10^{-10} . Nonetheless, increasing the number of quadrature points in the ST scheme did improve its accuracy. This indicates a better performance in engineering problems with more integration points, although the method is inevitably expensive.

The LC1 scheme, like the LFEM, only passed the linear patch test and failed the quadratic one. This means that the method only has the ability to reproduce a linear displacement field and, particularly, a constant strain field. Its incapability to reproduce a linear strain field should limit its stabilization effects in strain fields (or the stress fields in elastic case) for the ST1 scheme. However, its stabilization in the displacement fields for the ST1 scheme should be obvious. In addition, the convergence rates for both LC1 and LFEM should be similar, especially in displacement fields, because both of them only passed the linear patch test.

The proposed QC3 scheme is the only method that can pass both the linear and the quadratic patch tests. Therefore, its better performance in terms of accuracy, convergence rates, and stability than other methods is expected. Particularly, it should have better convergence properties and stability in stress/strain fields than the LC1 scheme, which corresponds to the SCNI [3].

The aforementioned judgments for all the methods based on the observations in the studied patch tests will be further demonstrated and validated by the following numerical examples.

6.2. Pressure-loaded half plane

Figure 2(a) shows the problem configuration and the exact solutions for the displacement, and stress fields are given in [2, 13]. The numerical model is a $3a \times 3a$ domain with $a = 1$, as shown in Figure 2(b). The symmetric boundary condition is applied along the y -axis, that is, the displacement is fixed in the x -direction and free in the y -direction. The displacements along $y = 3$ and the tractions along $x = 3$ are prescribed in accordance with the exact solutions.

First, six uniform grids, that is, 7×7 , 13×13 , 16×16 , 25×25 , 31×31 , and 49×49 , are used for the convergence study, and the corresponding ‘mesh’ size for these six grids are $h = 0.5, 0.25, 0.2, 0.125, 0.1, 0.0625$, respectively. The results are plotted in Figure 3. For this problem with uniform grids, all the tested methods are convergent in both displacement and energy. Even the ST1 scheme, which is a direct one-point integration method, exhibits convergence, although it results relatively large errors. This is also observed in [2, 13] for the direct nodal integration method.

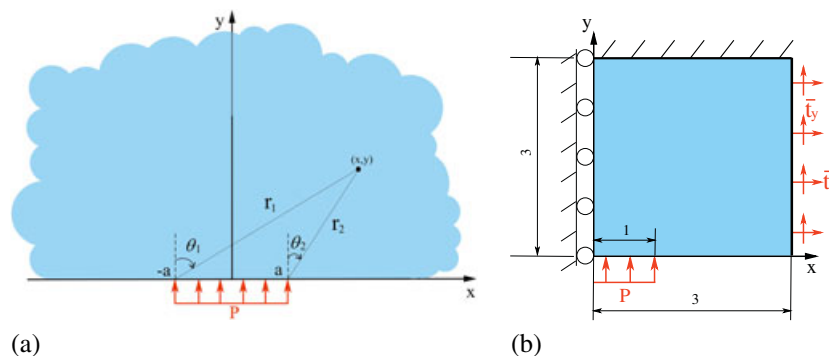


Figure 2. Pressure-loaded half plane problem: (a) schematic diagram; (b) solution domain.

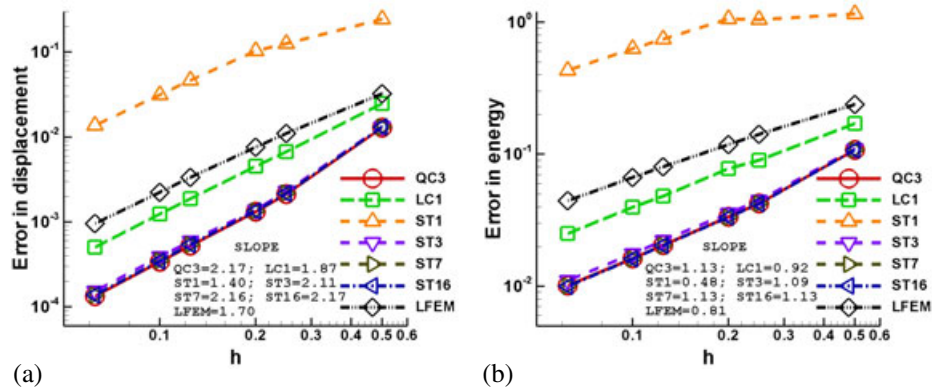


Figure 3. Convergence of the pressure-loaded half plane problem in regular nodal configuration: (a) displacement; (b) energy.

However, as shown in Figure 4, it does not show convergence in irregular nodal configurations, which are constructed by the perturbation given in Equation (49) to the uniform grids. Even the direct three-point integration method, that is, the ST3 scheme, in the case of non-uniform grids, does not show convergence.

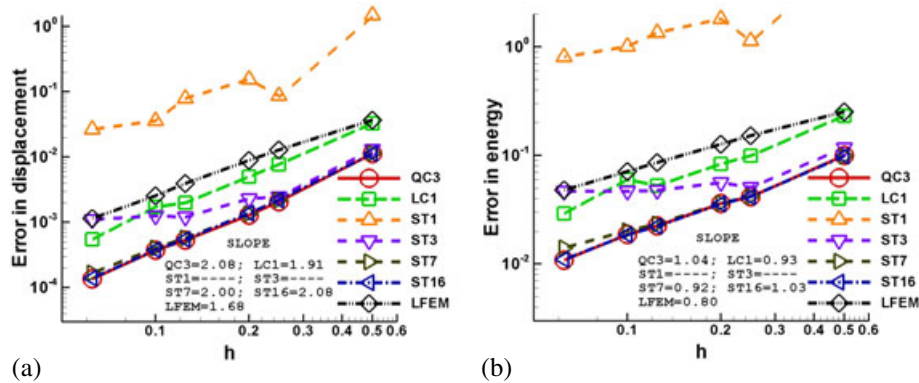


Figure 4. Convergence of the pressure-loaded half plane problem in irregular nodal configuration: (a) displacement; (b) energy.

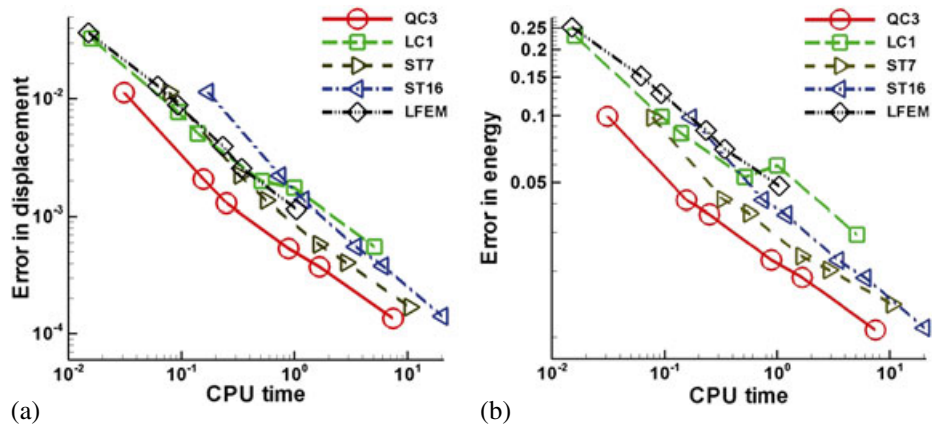


Figure 5. Computational efficiency of the pressure-loaded half plane problem in irregular nodal configuration in terms of (a) displacement and (b) energy.

The other five schemes show convergence in both uniform and non-uniform grids. Among them, the LC1 shows comparable convergence rate with the LFEM but a little more accurate. The developed QC3 scheme in this example performs almost the same as SH7 and SH16 in accuracy and convergence. Their convergence rates are only slightly higher than LC1 and LFEM, but they are the most accurate methods.

To compare efficiency, both the computational speed, that is, the CPU time, and the achieved accuracy should be taken into consideration. The CPU time cost is recorded for the five convergent methods and the accuracy–CPU time curves are plotted in Figure 5. QC3 is the most efficient scheme among all the five methods. Particularly, it has the same accuracy as ST16 but costs much less CPU time, for example, 7 s by QC3 in comparison with 20 s by ST16 for the finest grid.

Figure 6 shows the x -displacement fields by the tested methods with non-uniform grids. The ST1 scheme presents oscillations that lead to its poor convergence as shown in Figure 4. The LC1 scheme, which, like the ST1 scheme, also employs only the center of the triangle element as the evaluation point, shows smooth contour. This demonstrates its stabilization effects for the displacement field. Such oscillations can also be removed by increasing the number of integration points as ST7 and ST16 schemes as shown in Figure 6(e) and (f). The developed QC3 shows nicely smooth displacement field, and no oscillation presents while the contour by the ST3 scheme is not that smooth.

The σ_{xx} stress fields using the non-uniform grids are compared in Figure 7. QC3 shows perfectly smooth stress field, whereas the ST3 scheme results oscillatory σ_{xx} field. Both schemes employ the same three evaluation points per background triangle element; the only difference is that QC3 uses the corrected (smoothed) nodal derivatives computed in Equation (32) instead of the standard MLS nodal derivatives employed by ST3 scheme. The advantage of the smoothed nodal derivatives over the standard ones is clearly demonstrated in the comparison of Figure 7(a) and (d).

Also note that a mild oscillation presents in the stress field by the LC1 scheme as shown in Figure 7(b). Although such oscillation is not as severe as the stress field given by ST1 as shown in

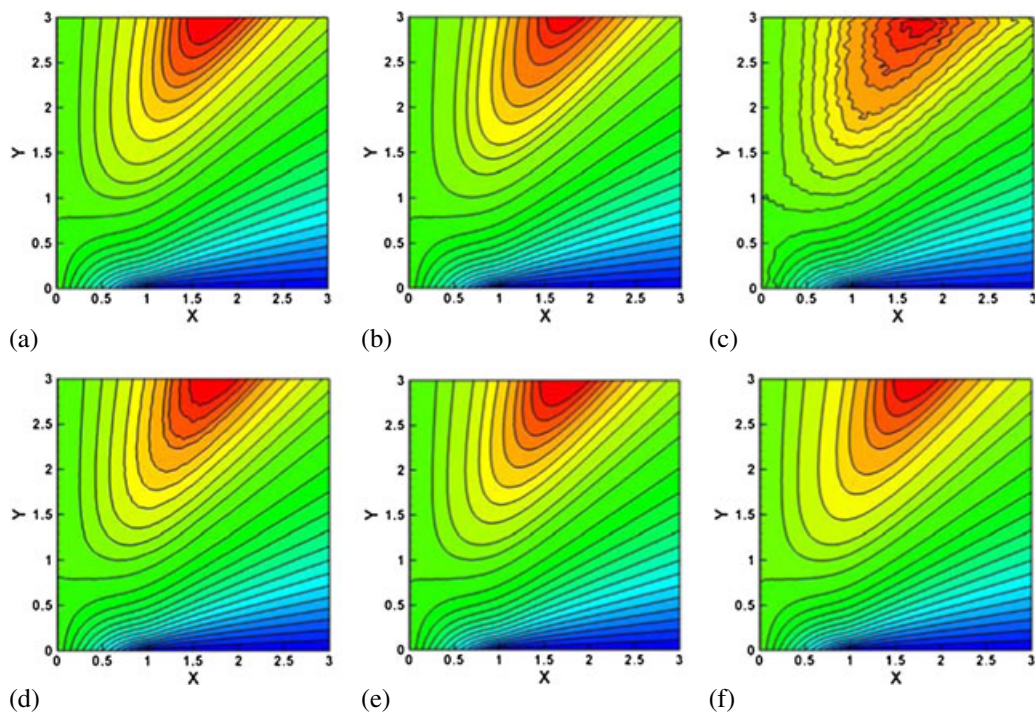


Figure 6. X -displacement fields of the pressure-loaded half plane problem in irregular nodal configuration by EFG with the integration schemes of (a) QC3, (b) LC1, (c) ST1, (d) ST3, (e) ST7, and (f) ST16.

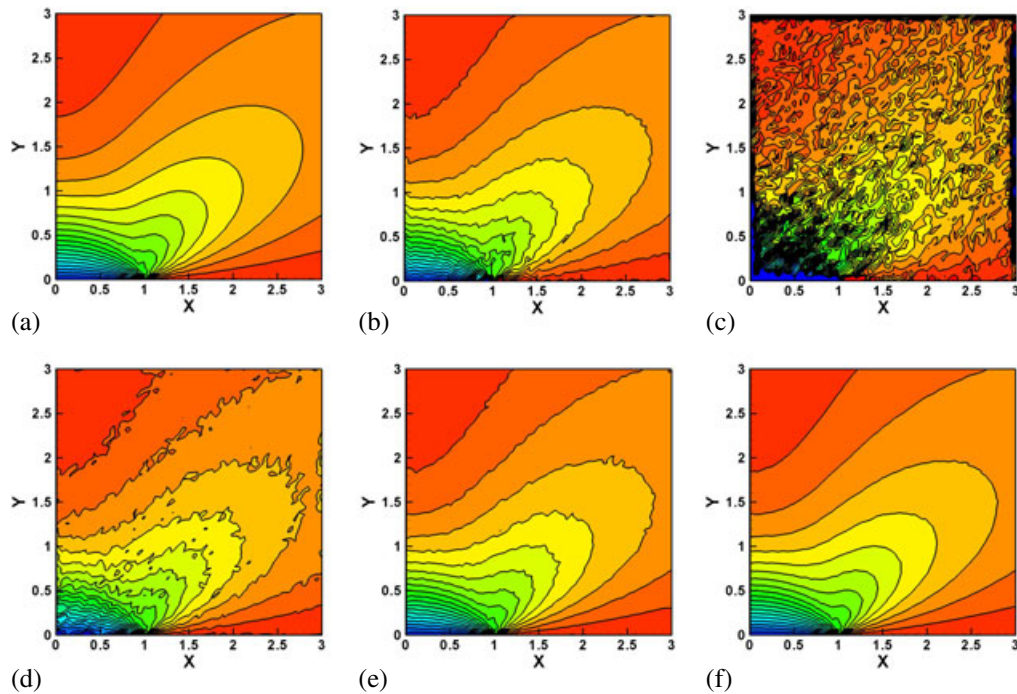


Figure 7. σ_{xx} stress fields of the pressure-loaded half plane problem in irregular nodal configuration by EFG with the integration schemes of (a) QC3, (b) LC1, (c) ST1, (d) ST3, (e) ST7, and (f) ST16.

Figure 7(c), it still deteriorates the accuracy of the LC1 scheme in both displacement and energy in comparison with the QC3 as shown in Figure 4. The comparison between the stress field by QC3 and the ones by ST3 and LC1 demonstrates the importance and the effects of the satisfaction of the quadratic DDC defined in Equation (30) with $\mathbf{q}(\mathbf{x}) = [1 \ x \ y]^T$.

6.3. Plate with a hole

As shown in Figure 8(a), this example is an infinite plate with a hole of radius a centered at the origin and loaded at infinity by $\sigma_{xx} = T$, $\sigma_{yy} = \sigma_{xy} = 0$. The exact solution of this problem has been given in many papers, for example, [2].

Because of twofold symmetry, only the first quadrant with $a = 1$ is modeled. The solution domain and the boundary conditions are shown in Figure 8(b). $u_x = 0$ along the line $x = 0$ and $u_y = 0$

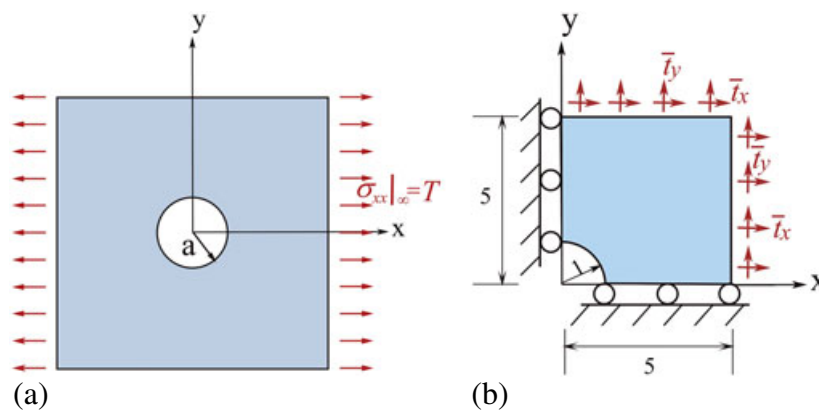


Figure 8. Plate with a hole problem: (a) schematic diagram; (b) solution domain.

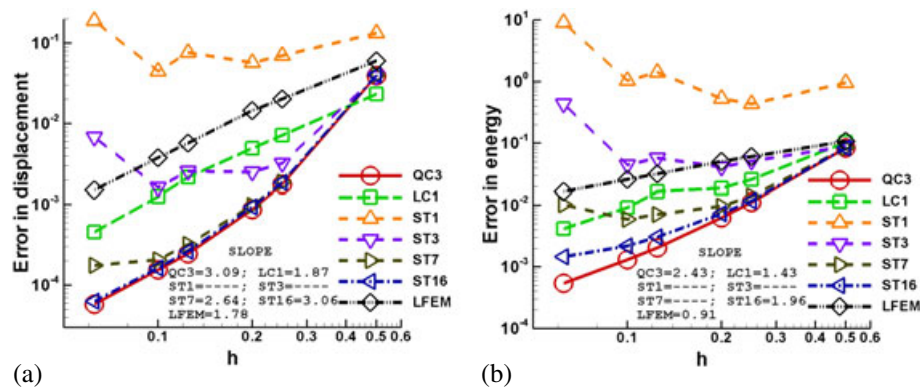


Figure 9. Convergence of the plate with a hole problem: (a) displacement; (b) energy.

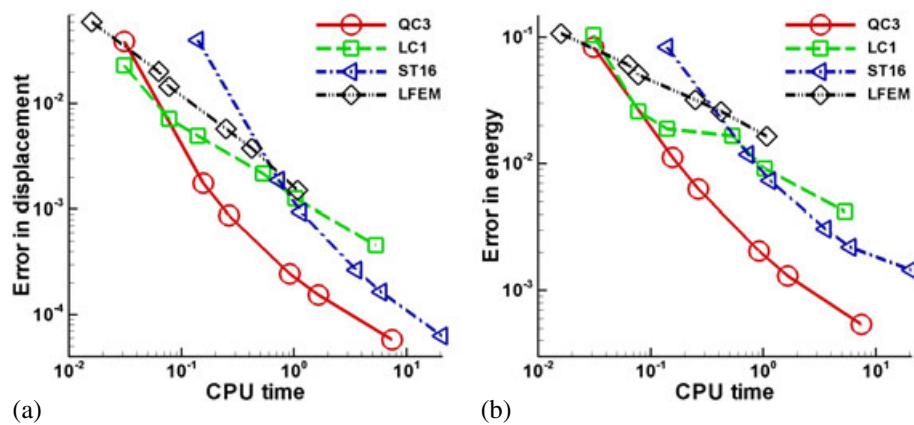


Figure 10. Computational efficiency of the plate with a hole problem in terms of (a) displacement and (b) energy.

along the line $y = 0$ are applied as the essential boundary conditions. The tractions are prescribed on the other two boundaries according to the exact solutions.

Six grids given in [13] are used to study the convergence, and the results are shown in Figure 9. The schemes ST1 and ST3 do not show convergence for this problem. ST7 displays some convergence when the grids are coarse; however, its convergence is lost when the grids become very dense.

The other four methods are convergent. Again, the LC1 scheme shows a similar convergence rate in displacement with the LFEM but more accurate. For the energy, LC1 is more accurate and converges faster than LFEM.

The proposed QC3 is the most accurate scheme with the highest convergence rate in both displacement and energy. Although the scheme ST16 shows comparable convergence rate and accuracy in displacement, its performance in energy is not as good as QC3. In addition, ST16 consumes more CPU time than QC3. This is shown in Figure 10. Obviously, QC3 is the most efficient method.

It is noted that the proposed QC3 performs much better than the LC1 scheme in accuracy, convergence, and efficiency as shown in Figures 9 and 10. Particularly, the convergence rates for QC3 is 3.09 in displacement and 2.43 in energy, whereas for LC1, they are only 1.87 in displacement and 1.43 in energy. The superiority of QC3 over LC1 comes from its satisfaction of the quadratic DDC. In contrast, LC1 only meets the linear DDC.

Figure 11 shows the y -displacement fields. Once again, in comparison with the ST1 scheme, LC1 displays a smooth contour, which manifests its stabilization effect for displacement field. However, its stabilization for stress field is not enough, as shown in Figure 12. A mild instability is observed

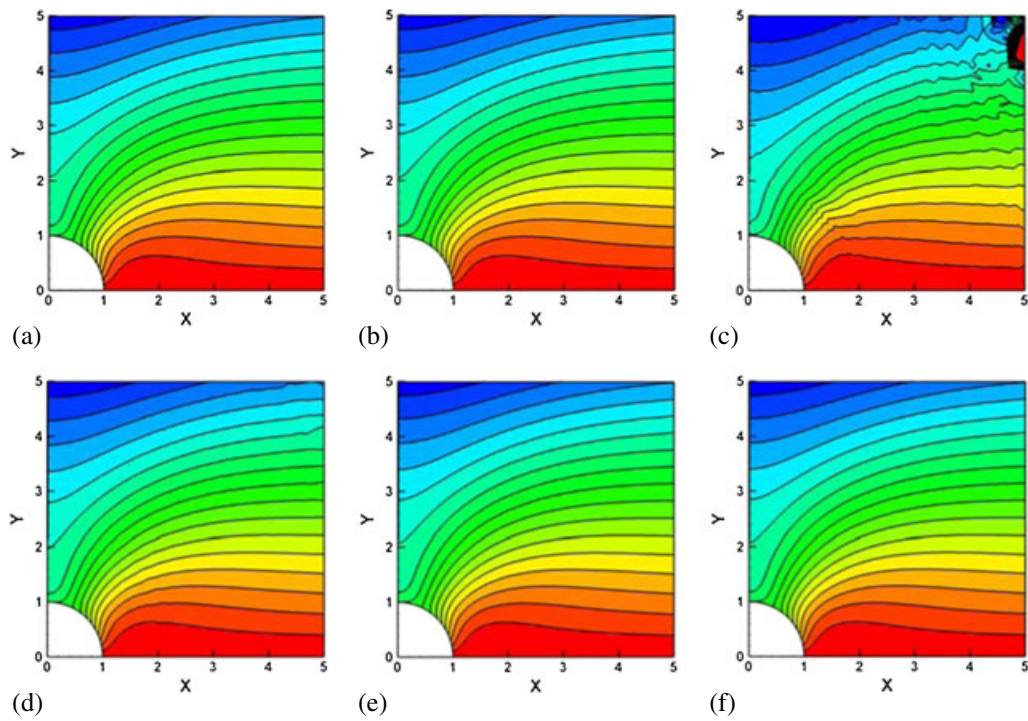


Figure 11. Y displacement fields of the plate with a hole problem by EFG with the integration schemes of: (a) QC3; (b) LC1; (c) ST1; (d) ST3; (e) ST7; (f) ST16.

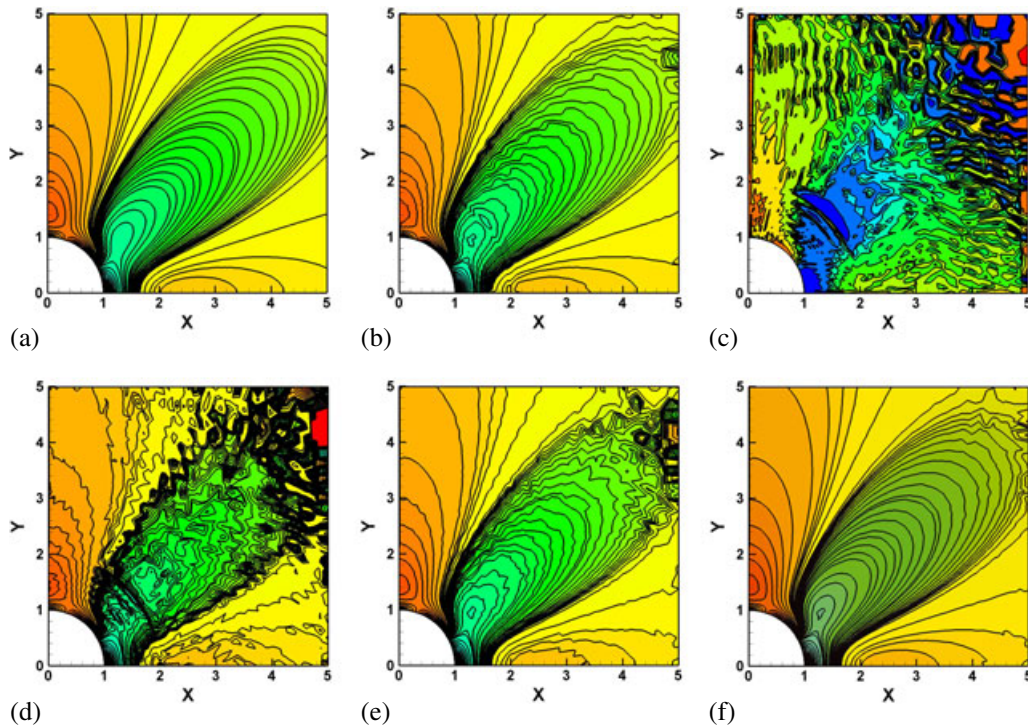


Figure 12. σ_{yy} stress fields of the plate with a hole problem by EFG with the integration schemes of: (a) QC3; (b) LC1; (c) ST1; (d) ST3; (e) ST7; (f) ST16.

in the stress computed by LC1. In contrast, the proposed QC3 scheme shows a perfectly smooth stress field, which is the best result among all the methods.

6.4. Cantilever beam

A cantilever beam with length L and height D , as shown in Figure 13, is next examined. The beam is subjected to a parabolic traction at the free end. The exact solution to this problem is well known; see [2, 7]. For this study, we set $L = 10m$ and $D = 1m$. The nonzero displacements in accordance with the exact solutions are prescribed at $x = 0$ as the essential boundary conditions. The traction given by the theoretical stress field is applied at $x = L$.

Five uniform grids, which respectively consist of 63, 306, 729, 1111, and 2737 evenly distributed nodes, are first employed in the convergence study, and the results are plotted in Figure 14. Once again, even the ST1 scheme displays some convergence in these uniform grids. However, for the

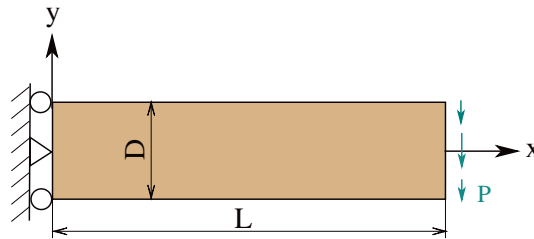


Figure 13. Schematic diagram of the cantilever beam problem.

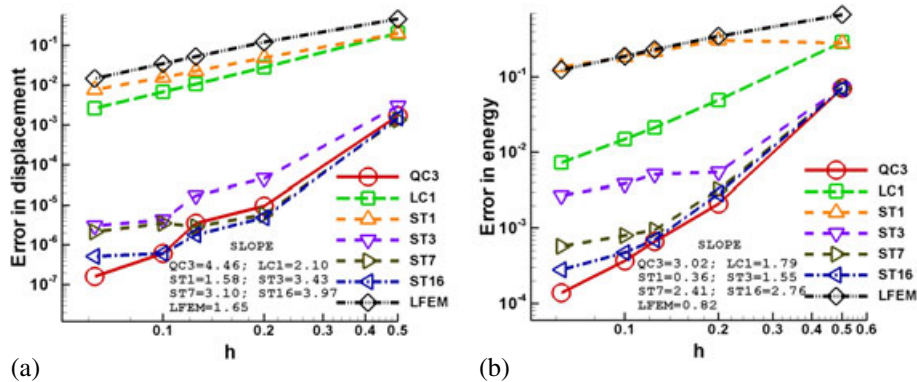


Figure 14. Convergence of the cantilever beam problem in regular nodal configuration: (a) displacement; (b) energy.

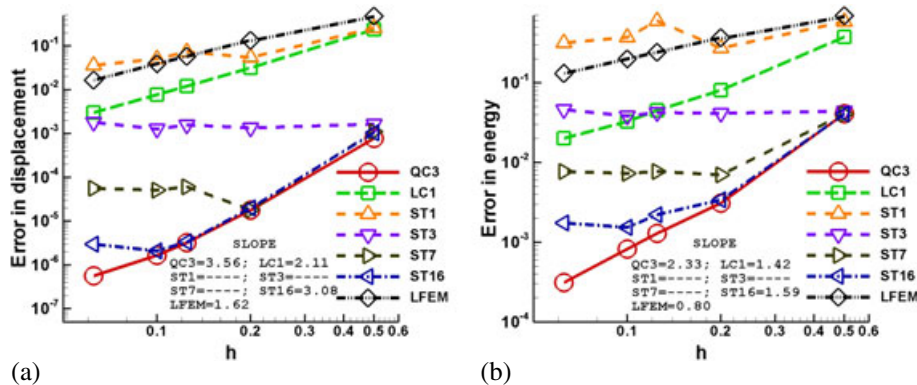


Figure 15. Convergence of the cantilever beam problem in irregular nodal configuration: (a) displacement; (b) energy.

non-uniform grids, only QC3, LC1, and LFEM show convergence as shown in Figure 15. The ST16 scheme shows nice convergence for the coarse grids. However, when the grid becomes very dense, its convergence is lost.

It is noted that the LFEM, although it is convergent, displays relatively large errors in this example, especially in energy. LC1, once again, shows a comparable convergence rate to LFEM and a little more accurate in displacement. Its performance in energy is evidently better than LFEM. Its accuracy in energy for the finest grid is about 10 times better than LFEM.

However, LC1 cannot even compete with the proposed QC3 scheme for this example. The convergence rates of QC3 are 3.56 in displacement and 2.33 in energy, which are much better than LC1's 2.11 in displacement and 1.42 in energy. The errors resulted by QC3 for the finest grid are on the order of 10^{-7} in displacement and 10^{-4} in energy, whereas LC1's errors are only on the order of 10^{-3} in displacement and 10^{-2} in energy. In other words, for this example, QC3 is more accurate than LC1 10 000 times in displacement and 100 times in energy.

The efficiency is also compared in Figure 16. Clearly, QC3 is the most efficient method and is much more efficient than LC1. Actually, the difference between the curves corresponding to these two methods in Figures 15 and 16 is huge, especially in the displacement field.

6.5. Manufactured problem with non-constant body force

The body force does not present in the last four examples, except in the quadratic patch test where the body force is constant. The purpose of this example is to test the performance of all the methods when a nonconstant body force appears.

This example is manufactured with the body force given by

$$\mathbf{b} = \begin{Bmatrix} (\sin x \cos y)\mathbf{D}(1, 1) - (e^x e^y)\mathbf{D}(1, 2) - (e^x e^y - \sin x \cos y)\mathbf{D}(3, 3) \\ (\cos x \sin y)\mathbf{D}(2, 1) - (e^x e^y)\mathbf{D}(2, 2) - (e^x e^y - \cos x \sin y)\mathbf{D}(3, 3) \end{Bmatrix}. \quad (53)$$

The exact solution to this problem is

$$u_x = \sin x \cos y \quad u_y = e^x e^y, \quad (54)$$

and the exact stress field is

$$\begin{Bmatrix} \sigma_{xx} \\ \sigma_{yy} \\ \sigma_{xy} \end{Bmatrix} = \begin{Bmatrix} \mathbf{D}(1, 1) \cos x \cos y + \mathbf{D}(1, 2)e^x e^y \\ \mathbf{D}(2, 1) \cos x \cos y + \mathbf{D}(2, 2)e^x e^y \\ \mathbf{D}(3, 3)(e^x e^y - \sin x \sin y) \end{Bmatrix}. \quad (55)$$

The solution domain is 2×2 . The displacement along the whole boundary is prescribed in accordance with the exact solution given in Equation (54). Six grids, that is, 5×5 , 9×9 , 11×11 , 17×17 ,

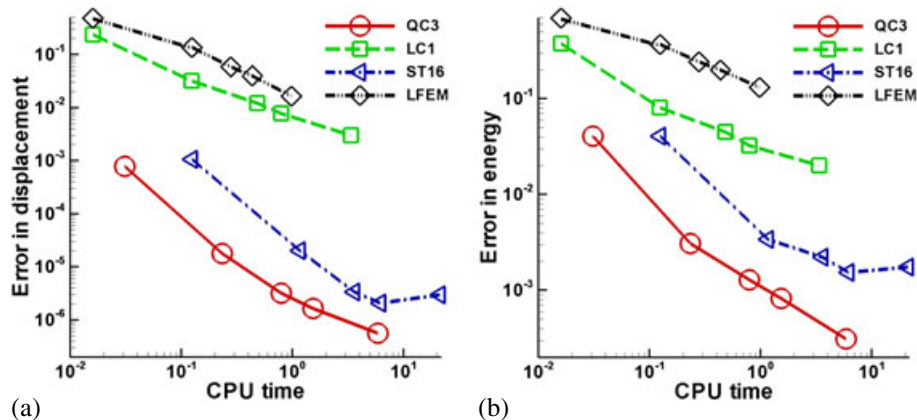


Figure 16. Computational efficiency of the cantilever beam problem in irregular nodal configuration in terms of (a) displacement and (b) energy.

21×21 , and 33×33 , are employed to study the convergence. Both uniform and non-uniform grids are tested, and the results are plotted in Figures 17 and 18, respectively. In addition, the efficiency is also compared in Figure 19. The proposed QC3 scheme is, once again, the most efficient and accurate method with the highest convergence rate in both displacement and energy. For the non-uniform grids, its convergence rates in displacement and energy are, respectively, about two to three times better than LC1. This is a huge improvement. ST16 also shows good accuracy and convergence rate

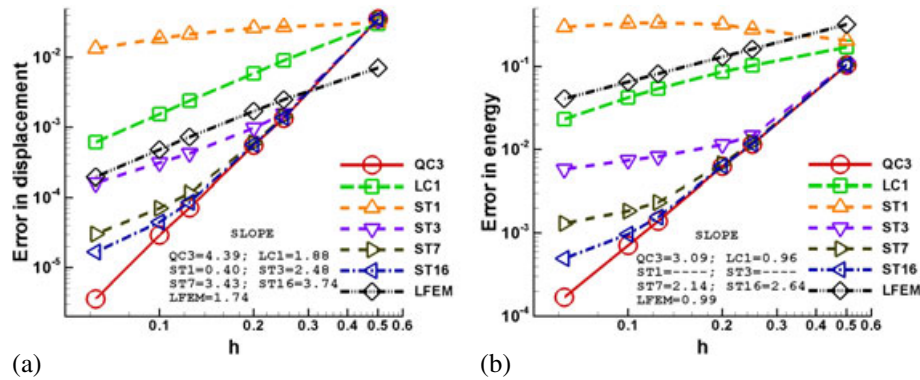


Figure 17. Convergence of the manufactured problem with nonconstant body force in regular nodal configuration: (a) displacement; (b) energy.

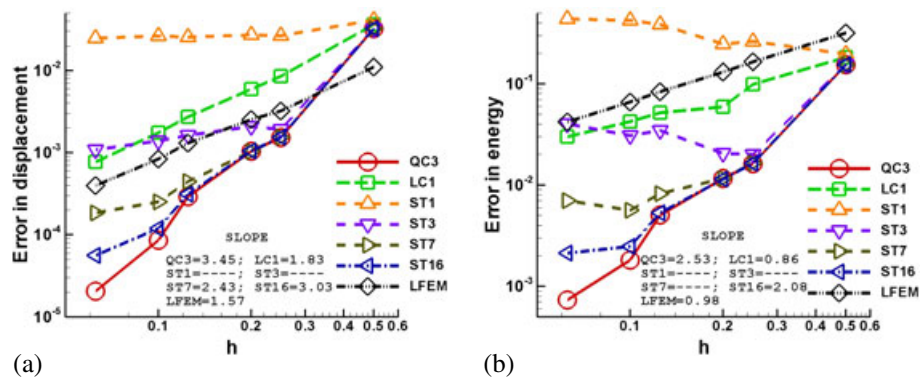


Figure 18. Convergence of the manufactured problem with nonconstant body force in irregular nodal configuration: (a) displacement; (b) energy.

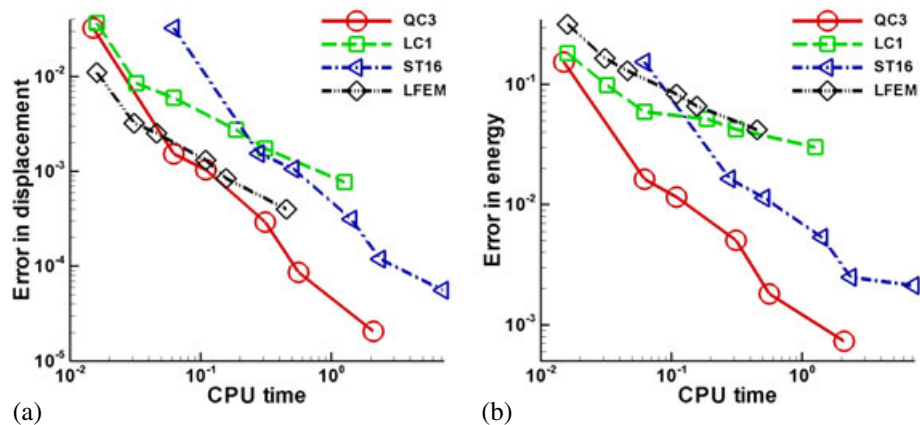


Figure 19. Computational efficiency of the manufactured problem with nonconstant body force in irregular nodal configuration in terms of (a) displacement and (b) energy.

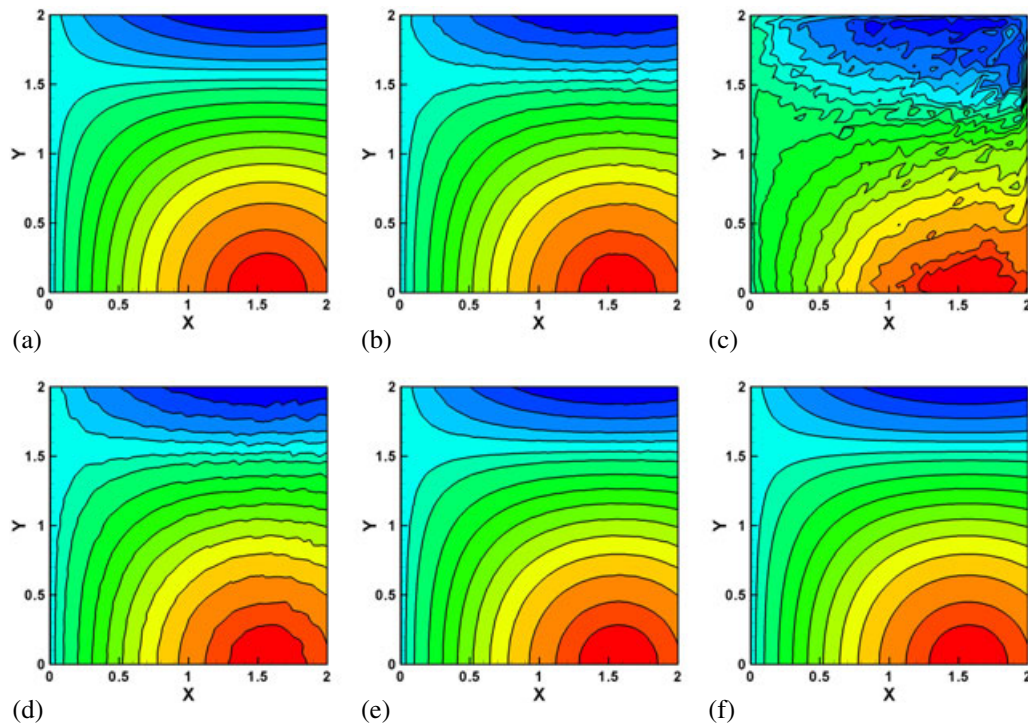


Figure 20. X -displacement fields of the manufactured problem with nonconstant body force in irregular nodal configuration by EFG with the integration schemes of (a) QC3, (b) LC1, (c) ST1, (d) ST3, (e) ST7, and (f) ST16.

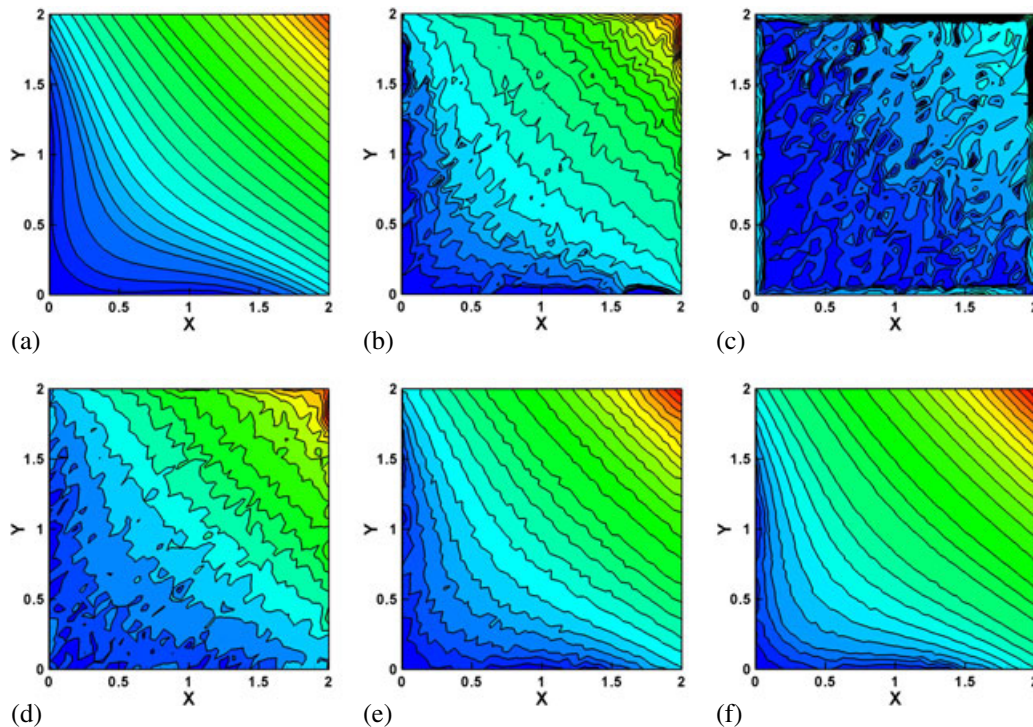


Figure 21. σ_{xx} stress fields of the manufactured problem with nonconstant body force in irregular nodal configuration by EFG with the integration schemes of (a) QC3, (b) LC1, (c) ST1, (d) ST3, (e) ST7, and (f) ST16.

for this example. However, its convergence in the region of fine grids deteriorates, and it is not as accurate as QC3. The other three ST schemes are not convergent for the non-uniform grids. But the effects of increasing the number of integration points on improving the convergence and accuracy are clearly demonstrated in Figure 18 by the comparison among all the ST schemes.

It is noted that, in the last three examples, LC1 always performs a little better than LFEM in terms of convergence rates, accuracy, and efficiency. But it is not the case for this example. As shown in Figure 18, for the six grids, LFEM is always more accurate than LC1 in displacement. Although LC1 is still more accurate than LFEM in energy, their accuracies are almost the same for the finest grid. We attribute this to the poor integration for the body force in LC1 because one point per cell (triangle element) is obviously not enough for such nonpolynomial body force given in Equation (53). In contrast, QC3 uses three points per cell to integrate the body force and performs much better than LC1, as shown in Figure 18.

This effect is further demonstrated by the displacement and stress contours shown in Figures 20 and 21, respectively. This time, LC1 shows a mild instability even in displacement field where its solutions to the last three examples are always stable and smooth. Things get even worse in its stress field as shown in Figure 21(b): quite severe oscillations present. In contrast, for the last three examples that do not include body forces, only mild instabilities are observed in the stress fields given by LC1. As mentioned earlier, such mild instability in the stress field solved by LC1 is due to its lack of the quadratic DDC for the nodal derivatives. The results of this example clearly show that the poor one-point integration for the body force in LC1 magnifies the consequence of its lack of quadratic DDC. Because of these reasons, LC1 almost cannot be used for these kind of problems where nonconstant body force presents.

In contrast, the proposed QC3 still shows stable solutions in both displacement and stress fields. Particularly, its stress solution is the best and smoothest result among all the tested methods. Thus, QC3 can be safely applied to the problems with nonconstant body force.

7. CONCLUSIONS

In this paper, the consistency of the derivatives of nodal shape functions in meshfree Galerkin methods is studied and a new framework is proposed. Besides the DAC, which is well known in the community, the DDC is introduced as a necessary condition to be met by nodal derivatives. In the proposed framework, by using one point in each integration cell and enforcing the linear DDC, the method LC1 similar to the SCNI [3] results without using the strain smoothing technique. The major innovation of this work is the proposed QC3 scheme, which uses three evaluation points in each background triangle element to enforce the quadratic DDC. The main features of the proposed QC3 are the following:

1. It uses background triangle elements for domain integrations.
2. In each element, three integration points for the domain integration are employed along with two Gauss points on each edge of the element for boundary integration.
3. The derivatives of the nodal shape functions at the three integration points are computed by the satisfaction of the quadratic DDC.
4. It also meets the quadratic DAC, and therefore, it is QC.

Patch tests and another four examples are used to test the developed QC3 scheme thoroughly and compare its numerical performance with the existing LC1, LFEM, and the standard triangle quadratures called ST schemes in this study. The major findings are as follows.

1. Among all the methods compared in this paper, QC3 is the only one that can pass both the linear and the quadratic patch tests. It is also the most accurate and efficient method with the highest convergence rates in both displacement and energy (strain or stress) fields for all the four examples. It is stable, and no oscillation presents in displacement or in stress fields for all the tested cases. It performs much better than LC1 and LFEM in terms of accuracy, convergence, and efficiency.

2. LC1, like SCNI [3], is a first-order method that only passes the linear patch test and fails the quadratic one. Generally, it performs similar to the LFEM even if the MLS approximation is quadratic. In comparison with the direct one-point quadrature, that is, ST1 scheme in this paper, it shows good stabilization for displacement fields, and its solution is quite smooth. However, its stabilization for the stress field is not enough, and a mild instability usually presents. LC1 performs even worse when nonconstant body force appears. Severe oscillations present in stress and a mild instability even presents in displacement.
3. EFG with standard triangle quadratures (ST schemes) passes neither the linear patch test nor the quadratic one. Its numerical performance improves with increasing number of quadrature points. The resulting method usually shows substantially good accuracy, stability, and convergence but relatively poor efficiency compared with QC3. Its convergence rates deteriorate for dense grids, and sometimes, it is not convergent. These conclusions for the ST schemes using background triangle elements should also apply to the domain Gauss quadratures using background quadrilateral elements.
4. Passing the linear patch test is very important for convergence. Although there is some controversy as to whether passing the linear patch test is necessary and sufficient for convergence, the numerical studies in this paper show that the three methods, that is, QC3, LC1, and LFEM, which passed the linear patch test, show convergence for all the tested examples, whereas the ST schemes that did not pass the linear patch test cannot ensure the convergence for all the tested cases.

Although the proposed QC3 scheme shows amazing superiority over the existing methods for quadratic approximations, this is only demonstrated for the simple elastic problems. Its performance in complicated problem such as large deformation is still an open topic, and more investigation and research work are required. Incidentally, QC here not only is the abbreviation of 'quadratically consistent' but also implies the 'quasi-conforming' technique in the spirit of Tang *et al.* [22–24].

ACKNOWLEDGEMENTS

The authors are pleased to acknowledge the support of this work by the National Natural Science Foundation of China through grant nos. 11102036, 11072046, and 11072051, the National Key Basic Research and Development Program (973 Program, no. 2010CB731502), the 111 Project of China (no.B08014), and the Fundamental Research Funds for the Central Universities through grant nos. DUT10RC(3)84 and DUT12LK08.

REFERENCES

1. Belytschko T, Lu Y, Gu L. Element-free Galerkin methods. *International Journal for Numerical Methods in Engineering* 1994; **37**(2):229–256.
2. Beissel S, Belytschko T. Nodal integration of the element-free Galerkin method. *Computer Methods in Applied Mechanics and Engineering* 1996; **139**(1):49–74.
3. Chen J, Wu C, Yoon S, You Y. A stabilized conforming nodal integration for Galerkin mesh-free methods. *International Journal for Numerical Methods in Engineering* 2001; **50**(2):435–466.
4. Chen J, Yoon S, Wu C. Non-linear version of stabilized conforming nodal integration for Galerkin mesh-free methods. *International Journal for Numerical Methods in Engineering* 2002; **53**(12):2587–2615.
5. Wang D, Chen J. A hermite reproducing kernel approximation for thin-plate analysis with sub-domain stabilized conforming integration. *International Journal for Numerical Methods in Engineering* 2008; **74**(3):368–390.
6. Puso M, Chen J, Zywicki E, Elmer W. Meshfree and finite element nodal integration methods. *International Journal for Numerical Methods in Engineering* 2008; **74**(3):416–446.
7. Liu G, Zhang G, Wang Y, Zhong Z, Li G, Han X. A nodal integration technique for meshfree radial point interpolation method (NI-RPIM). *International Journal of Solids and Structures* 2007; **44**(11):3840–3860.
8. Bonet J, Kulasegaram S. Correction and stabilization of smooth particle hydrodynamics methods with applications in metal forming simulations. *International Journal for Numerical Methods in Engineering* 2000; **47**(6):1189–1214.
9. Dyka C, Ingel R. An approach for tension instability in smoothed particle hydrodynamics (SPH). *Computers & Structures* 1995; **57**(4):573–580.
10. Dyka C, Randles P, Ingel R. Stress points for tension instability in SPH. *International Journal for Numerical Methods in Engineering* 1997; **40**(13):2325–2341.
11. Rabczuk T, Belytschko T, Xiao S. Stable particle methods based on Lagrangian kernels. *Computer Methods in Applied Mechanics and Engineering* 2004; **193**(12):1035–1063.

12. Fries T, Belytschko T. Convergence and stabilization of stress-point integration in mesh-free and particle methods. *International Journal for Numerical Methods in Engineering* 2008; **74**(7):1067–1087.
13. Duan Q, Belytschko T. Gradient and dilatational stabilizations for stress-point integration in the element-free Galerkin method. *International Journal for Numerical Methods in Engineering* 2009; **77**(6):776–798.
14. Atluri S, Shen S. *The Meshless Local Petrov–Galerkin (MLPG) Method*. Tech Science Press: Duluth, GA, USA, 2002.
15. De S, Bathe K. The method of finite spheres with improved numerical integration. *Computers & Structures* 2001; **79**(22):2183–2196.
16. Kwon K, Park S, Youn S. The support integration scheme in the least-squares mesh-free method. *Finite Elements in Analysis and Design* 2006; **43**(2):127–144.
17. Liu Y, Belytschko T. A new support integration scheme for the weakform in mesh-free methods. *International Journal for Numerical Methods in Engineering* 2010; **82**(2):699–715.
18. Krongauz Y, Belytschko T. Consistent pseudo-derivatives in meshless methods. *Computer Methods in Applied Mechanics and Engineering* 1997; **146**(3):371–386.
19. Liu G, Dai K, Nguyen T. A smoothed finite element method for mechanics problems. *Computational Mechanics* 2007; **39**(6):859–877.
20. Liu G, Nguyen T, Dai K, Lam K. Theoretical aspects of the smoothed finite element method (SFEM). *International Journal for Numerical Methods in Engineering* 2007; **71**(8):902–930.
21. Nguyen-Xuan H, Bordas S, Nguyen-Dang H. Smooth finite element methods: convergence, accuracy and properties. *International Journal for Numerical Methods in Engineering* 2008; **74**(2):175–208.
22. Tang L, Chen W, Liu Y. Quasi-conforming elements for finite element analysis. *Journal of Dalian University of Technology* 1980; **19**(2):19–35.
23. Tang L, Chen W, Liu Y. Formulation of quasi-conforming element and Hu-Washizu principle. *Computers & Structures* 1984; **19**(1):247–250.
24. Tang L, Liu Y. Quasi-conforming element techniques for penalty finite element methods. *Finite Elements in Analysis and Design* 1985; **1**(1):25–33.
25. Fernández-Méndez S, Huerta A. Imposing essential boundary conditions in mesh-free methods. *Computer Methods in Applied Mechanics and Engineering* 2004; **193**(12):1257–1275.
26. Dunavant D. High degree efficient symmetrical Gaussian quadrature rules for the triangle. *International Journal for Numerical Methods in Engineering* 1985; **21**(6):1129–1148.